Measurement of the $\Sigma\pi$ photoproduction line shapes near the $\Lambda(1405)$

K. Moriya,[1, *] R.A. Schumacher,[1, †] K.P. Adhikari,[28] D. Adikaram,[28] M. Aghasyan,[17] M.D. Anderson,[36] S. Anefalos Pereira,[17] J. Ball,[6] N.A. Baltzell,[2, 33] M. Battaglieri,[18] V. Batourine,[34, 23] I. Bedlinskiy,[21] M. Bellis,[1, ‡] A.S. Biselli,[10, 1] J. Bono,[11] S. Boiarinov,[34] W.J. Briscoe,[14] V.D. Burkert,[34] D.S. Carman,[34] A. Celentano,[18] S. Chandavar,[27] G. Charles,[6] P.L. Cole,[15] P. Collins,[5] V. Crede,[12] A. D'Angelo,[19, 31] N. Dashyan,[39] E. De Sanctis,[17] R. De Vita,[18] A. Deur,[34] B. Dey,[1] C. Djalali,[33] D. Doughty,[7, 34] R. Dupre,[20] H. Egiyan,[34] L. El Fassi,[2] P. Eugenio,[12] G. Fedotov,[33, 32] S. Fegan,[18] R. Fersch,[7] J.A. Fleming,[9] N. Gevorgyan,[39] G.P. Gilfoyle,[30] K.L. Giovanetti,[22] F.X. Girod,[34, 6] J.T. Goetz,[27] W. Gohn,[8] E. Golovatch,[32] R.W. Gothe,[33] K.A. Griffioen,[38] M. Guidal,[20] K. Hafidi,[2] H. Hakobyan,[35, 39] C. Hanretty,[37] N. Harrison,[8] D. Heddle,[7, 34] K. Hicks,[27] D. Ho,[1] M. Holtrop,[25] C.E. Hyde,[28] Y. Ilieva,[33, 14] D.G. Ireland,[36] B.S. Ishkhanov,[32] E.L. Isupov,[32] H.S. Jo,[20] D. Keller,[37] M. Khandaker,[26] P. Khetarpal,[11] A. Kim,[23] W. Kim,[23] A. Klein,[28] F.J. Klein,[5] S. Koirala,[28] A. Kubarovsky,[29, 32] V. Kubarovsky,[34, 29] S.V. Kuleshov,[35, 21] N.D. Kvaltine,[37] K. Livingston,[36] H.Y. Lu,[1] I .J .D. MacGregor,[36] N. Markov,[8] M. Mayer,[28] M. McCracken,[1] B. McKinnon,[36] M.D. Mestayer,[34] C.A. Meyer,[1] M. Mirazita,[17] T. Mineeva,[8] V. Mokeev,[34, 32] R.A. Montgomery,[36] E. Munevar,[34] C. Munoz Camacho,[20] P. Nadel-Turonski,[34] R. Nasseripour,[22, 11] C.S. Nepali,[28] S. Niccolai,[20] G. Niculescu,[22] I. Niculescu,[22] M. Osipenko,[18] A.I. Ostrovidov,[12] L.L. Pappalardo,[16] R. Paremuzyan,[20] K. Park,[34, 23] S. Park,[12] E. Pasyuk,[34, 3] E. Phelps,[33] J.J. Phillips,[36] S. Pisano,[17] N. Pivnyuk,[21] O. Pogorelko,[21] S. Pozdniakov,[21] J.W. Price,[4] S. Procureur,[6] D. Protopopescu,[36] D. Rimal,[11] M. Ripani,[18] B.G. Ritchie,[3] G. Rosner,[36] P. Rossi,[17] F. Sabatié,[6] M.S. Saini,[12] C. Salgado,[26] D. Schott,[14] E. Seder,[8] H. Seraydaryan,[28] Y.G. Sharabian,[34] E.S. Smith,[34] G.D. Smith,[36] D.I. Sober,[5] S.S. Stepanyan,[23] S. Stepanyan,[34] P. Stoler,[29] I.I. Strakovsky,[14] S. Strauch,[33, 14] M. Taiuti,[18] W. Tang,[27] S. Taylor,[34] C.E. Taylor,[15] Ye Tian,[33] S. Tkachenko,[37] B. Torayev,[28] M. Ungaro,[34, 8, 29] B. Vernarsky,[1] A.V. Vlassov,[21] H. Voskanyan,[39] E. Voutier,[24] N.K. Walford,[5] D.P. Watts,[9] D.P. Weygand,[34] M. Williams,[1] N. Zachariou,[33] L. Zana,[25] J. Zhang,[34] Z.W. Zhao,[37] and I. Zonta[31]

(The CLAS Collaboration)

[1] *Carnegie Mellon University, Pittsburgh, Pennsylvania 15213*
[2] *Argonne National Laboratory, Argonne, Illinois 60439*
[3] *Arizona State University, Tempe, Arizona 85287-1504*
[4] *California State University, Dominguez Hills, Carson, California 90757, USA*
[5] *Catholic University of America, Washington, D.C. 20064*
[6] *CEA, Centre de Saclay, Irfu/Service de Physique Nucléaire, 91191 Gif-sur-Yvette, France*
[7] *Christopher Newport University, Newport News, Virginia 23606*
[8] *University of Connecticut, Storrs, Connecticut 06269*
[9] *Edinburgh University, Edinburgh EH9 3JZ, United Kingdom*
[10] *Fairfield University, Fairfield CT 06824*
[11] *Florida International University, Miami, Florida 33199*
[12] *Florida State University, Tallahassee, Florida 32306*
[13] *Università di Genova, 16146 Genova, Italy*
[14] *The George Washington University, Washington, DC 20052*
[15] *Idaho State University, Pocatello, Idaho 83209*
[16] *INFN, Sezione di Ferrara, 44100 Ferrara, Italy*
[17] *INFN, Laboratori Nazionali di Frascati, 00044 Frascati, Italy*
[18] *INFN, Sezione di Genova, 16146 Genova, Italy*
[19] *INFN, Sezione di Roma Tor Vergata, 00133 Rome, Italy*
[20] *Institut de Physique Nucléaire ORSAY, Orsay, France*
[21] *Institute of Theoretical and Experimental Physics, Moscow, 117259, Russia*
[22] *James Madison University, Harrisonburg, Virginia 22807*
[23] *Kyungpook National University, Daegu 702-701, Republic of Korea*
[24] *LPSC, Universite Joseph Fourier, CNRS/IN2P3, INPG, Grenoble, France*
[25] *University of New Hampshire, Durham, New Hampshire 03824-3568*
[26] *Norfolk State University, Norfolk, Virginia 23504*
[27] *Ohio University, Athens, Ohio 45701*
[28] *Old Dominion University, Norfolk, Virginia 23529*
[29] *Rensselaer Polytechnic Institute, Troy, New York 12180-3590*
[30] *University of Richmond, Richmond, Virginia 23173*
[31] *Universita' di Roma Tor Vergata, 00133 Rome Italy*
[32] *Skobeltsyn Nuclear Physics Institute, 119899 Moscow, Russia*
[33] *University of South Carolina, Columbia, South Carolina 29208*
[34] *Thomas Jefferson National Accelerator Facility, Newport News, Virginia 23606*
[35] *Universidad Técnica Federico Santa María, Casilla 110-V Valparaíso, Chile*

[36] *University of Glasgow, Glasgow G12 8QQ, United Kingdom*
[37] *University of Virginia, Charlottesville, Virginia 22901*
[38] *College of William and Mary, Williamsburg, Virginia 23187-8795*
[39] *Yerevan Physics Institute, 375036 Yerevan, Armenia*

(Dated: January 25, 2013)

The reaction $\gamma + p \rightarrow K^+ + \Sigma + \pi$ was used to determine the invariant mass distributions or "line shapes" of the $\Sigma^+\pi^-$, $\Sigma^-\pi^+$ and $\Sigma^0\pi^0$ final states, from threshold at 1328 MeV/c^2 through the mass range of the $\Lambda(1405)$ and the $\Lambda(1520)$. The measurements were made with the CLAS system at Jefferson Lab using tagged real photons, for center-of-mass energies $1.95 < W < 2.85$ GeV. The three mass distributions differ strongly in the vicinity of the $I = 0$ $\Lambda(1405)$, indicating the presence of substantial $I = 1$ strength in the reaction. Background contributions to the data from the $\Sigma^0(1385)$ and from $K^*\Sigma$ production were studied and shown to have negligible influence. To separate the isospin amplitudes, Breit-Wigner model fits were made that included channel-coupling distortions due to the $N\bar{K}$ threshold. A best fit to all the data was obtained after including a phenomenological $I = 1$, $J^P = 1/2^-$ amplitude with a centroid at 1394 ± 20 MeV/c^2 and a second $I = 1$ amplitude at 1413 ± 10 MeV/c^2. The centroid of the $I = 0$ $\Lambda(1405)$ strength was found at the $\Sigma\pi$ threshold, with the observed shape determined largely by channel-coupling, leading to an apparent overall peak near 1405 MeV/c^2.

I. INTRODUCTION

The $\Lambda(1405)$, situated just below $N\bar{K}$ threshold, has been an enigmatic state in the spectrum of strange baryons for decades. First seen in bubble chamber experiments in the 1960's [1], there have been remarkably few measurements of this state to date. The most prominent feature of the state is that its invariant mass spectrum, which we call the "line shape", has always been seen to be distorted from a Breit-Wigner form, indicating that there are strong dynamics at work that are not seen in more typical resonances. Almost all theories agree that this is due to the state's strong coupling to $N\bar{K}$, but the exact nature of this coupling is as yet unknown. Due to its mass being below the $N\bar{K}$ threshold, it is not possible to produce it directly in kaon beam experiments, so accessing this state experimentally has been a challenge compared to other strange baryon resonances. Precise measurements of the line shape should yield information on what dynamics play a significant role in the $\Lambda(1405)$, and lead to a deeper understanding of the additional amplitudes that may exist in this mass region.

A. Theories of the $\Lambda(1405)$

Explaining the mass of the $\Lambda(1405)$ has also proved to be a problem. The state does not fit well within the constituent quark model that has otherwise worked remarkably well for understanding the masses of low-lying baryon resonances [2]. Theoretical investigations into the nature of the $\Lambda(1405)$ were discussed from the days of its

—————

* Current address:Indiana University, Bloomington, Indiana 47405
† Contact: schumacher@cmu.edu
‡ Current address:Siena College, Loudonville, NY 12211

prediction by Dalitz and others [3], and there has been a surge of interest in recent years. Chiral unitary theory [4–6] combines chiral dynamics with unitarity constraints based on effective meson-baryon interactions. In this class of models, the $\Lambda(1405)$ is dynamically generated as a rescattering of all pseudo-scalar meson and octet baryon states that couple to it. Definite predictions have been made of what the line shape of the $\Lambda(1405)$ should be for photoproduction near threshold [7]. In this model the interference between a dominant isospin $I = 0$ amplitude and a smaller $I = 1$ amplitude causes the line shapes for each $\Sigma\pi$ channel to be different.

Further developments of the chiral unitary approach have shown that the $\Lambda(1405)$ may be composed of two $I = 0$ poles, whose couplings to various particle final states and whose initial-state populations differ according to the reaction under investigation [8–10]. The $\Lambda(1405)$ plays a special role in these theories as the archetype of a dynamically generated rescattering state, but the models also impinge on the nature of non-strange nucleon resonances such as the $N(1535)S_{11}$ and $N(1440)P_{11}$.

In another approach [11] the pair of states $\Sigma(1385)$ and $\Lambda(1405)$ are treated together in a kaon double-pole model with an explicit assumption of photon dissociation into a real K^+ and a virtual K^- as illustrated in Fig. 1. This model also made specific predictions for the mass distributions of $\Sigma\pi$ and $\Lambda\pi^0$ final states that we will mention later. In a meson exchange model [12] the $\Lambda(1405)$ is generated dynamically by the coherent addition of ω, ρ and scalar-meson exchanges. Here, too, it appears as a two-pole structure in the $N\bar{K}$ S_{01} partial wave.

Other theories see the $\Lambda(1405)$ as a bound state of $N\bar{K}$ [13] alone, and the dynamics that create it are expected to have significant repercussions on whether bound K^-pp states exist. In other views, the $\Lambda(1405)$ is pictured as a true 3-quark state [14], or as a negative-parity [15] or positive-parity [16] hybrid state.

The spectrum of $I = 1$ Σ excited states is also pre-

dicted to be quite different in different models. As discussed recently in Ref. [17], standard so-called quenched quark models put the $J^P = \frac{1}{2}^- \Sigma$ at about 1650 MeV/c^2, while an unquenched model that allows $[qq][qq]\bar{q}$ S-wave configurations expects it near 1380 MeV/c^2. Some evidence for a light negative-parity Σ has been discussed for several years [18–21]. In a different vein, meson-baryon dynamical models place a Σ^* $(1/2)^-$ near 1430 MeV/c^2 [22], 1475 MeV/c^2 [23], or 1620 MeV/c^2 [24]. It is therefore of interest to look for evidence of isospin one strength in the $\Sigma\pi$ system in the same neighborhood as the isospin zero $\Lambda(1405)$. Discovery of a resonant structure in that same mass range could be decisive in picking among models of baryonic excitations.

B. Experiments on the $\Lambda(1405)$

While there has been continual theoretical interest in the $\Lambda(1405)$, there have been remarkably few measurements made of this state, known for more than half a century and given a 4-star rating by the PDG [25]. Bubble chamber experiments using hadronic beams at Brookhaven [26] and CERN [27] have long been the only experiments to identify the line shape, and that with barely adequate statistics. The mass and width of the $\Lambda(1405)$ cited by the PDG are based primarily on these measurements.

In recent years, with the development of higher-statistics experimental capabilities, there has been a renewed interest in measuring the $\Lambda(1405)$. These include measurement of the $\Sigma^0\pi^0$ line shape in proton-proton collisions at COSY [28], measurement of the $\Sigma^\pm\pi^\mp$ line shapes in proton-proton collisions at HADES [29], and again the measurement of the $\Sigma^\pm\pi^\mp$ line shapes using photoproduction by LEPS [30, 31]. The LEPS measurement has some overlap with the energy used in our measurement, but due to limited statistics, their results depended on broad averaging over kinematics and line shape comparisons with existing theoretical curves, rather than on new and decisive fits to the data.

In this paper, we report results of a measurement with large statistics accumulated with the CLAS system in Hall B of Jefferson Lab. With good mass resolution for the $\Lambda(1405)$, we will show for the first time a measurement of all three $\Sigma\pi$ line shapes. The center-of-mass energies (W) in this experiment covered a wide range from near production threshold of the $\Lambda(1405)$ up to 2.85 GeV, which allowed us to measure the energy-dependence of the line shapes. The results are shown after summing the line shapes over all kaon production angles for each energy; another paper that is in preparation will show the differential cross sections for each energy [32].

The line shapes are differential in the $\Sigma\pi$ invariant mass, m, and extracted for nine bins in the initial state γp invariant energy W. We anticipate that the W dependence of the $I = 0$ and $I = 1$ contributions varies slowly.

This is because the data stem from an associated production experiment accompanied by a kaon, as opposed to a direct formation experiment, so that the connection of energy W to the properties of the excited strange resonance(s) is indirect. This is indicated in Fig. 1, for example, where the intermediate hyperon is construed to be created via an off-shell kaon as part of a t-channel interaction between the incoming photon and the target proton.
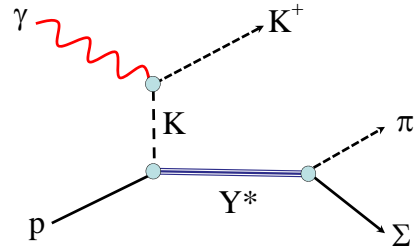

FIG. 1. (Color online) Creation of the three-body $K^+ \Sigma \pi$ final state via an intermediate hyperon in the reaction $\gamma + p \to K^+ + \Sigma + \pi$. In this particular example, a t-channel exchange enables an off-shell kaon to create a $\Lambda(1405)$ that is sub-threshold for on-shell $N\bar{K}$ reactions.

The outline of this paper is as follows. Sections II–IV present the details of the setup of the experiment, the event selection used to extract the yield of the various final states, the acceptance corrections and the data normalization. Section V describes our method of extracting the yield of signal events from the data, Section VI presents the line shape results for the three $\Sigma\pi$ final states, and Section VII discusses the systematic uncertainties and the methods used to test the reliability of the measurements. Section VIII explains the method used to fit the line shapes we obtained. In Section IX the outcome of fitting the mass distributions with this model is given, and we conclude with Section X.

II. EXPERIMENTAL SETUP

The data for this experiment were obtained during May and June of 2004 with the CLAS detector, located in Hall B at the Thomas Jefferson National Accelerator Facility The run, known as g11a, used a 40 cm unpolarized liquid hydrogen (LH2) target and an incoming unpolarized real-photon beam. Bremsstrahlung photons with an endpoint energy of 4.019 GeV were created via the CEBAF accelerator electron beam and a 10^{-4} radiation length gold foil. Electrons that radiated a photon were identified with the CLAS tagger [33] to obtain energy and timing information between 20% and 95% of

the endpoint energy.

Details of the CLAS detector can be found in Ref. [34]. Here we give a very brief description of the main components used in our analysis. CLAS was equipped with a superconducting toroidal magnet with six identical sectors surrounding the beam line. The field was selected to bend positive particles away from the beam line. A 34-layer drift chamber system in each sector provided charge and momentum information for charged particles. Momentum resolution $\delta p/p$ was $\approx 0.5\%$. The target was surrounded by a 24 element plastic scintillator Start Counter used in the trigger to select charged tracks leaving the target. Finally, a system of 342 time of flight (TOF) scintillators was used in the trigger which also determined the duration of flight of each charged particle. For the g11a run period, the trigger required a hit in the tagger system in coincidence with Start Counter and TOF hits in at least two of the six sectors. A sector trigger required hits in a Start Counter paddle and a TOF paddle within 150 ns of each other. With this setup, the g11a run accumulated over 20 billion events, including a large sample of excited hyperon states. More details of the setup and analysis can be found in Ref. [35].

III.   EVENT SELECTION

For reference, we include Fig. 2 to illustrate the various data-handling paths in this analysis. The main interest lies in the $\Sigma\pi$ final states of the hyperon decays, particularly $\Lambda(1405) \to \Sigma\pi$. The analysis channels can be divided into two main categories depending on the final charged particles detected. The first case is when a K^+, p, and π^- are detected, while the second is when a K^+, π^+, and π^- are detected. The main strong final states of interest are then $K^+\Sigma^+\pi^-$, $K^+\Sigma^0\pi^0$, $K^+\Sigma^-\pi^+$, and $K^+\Lambda\pi^0$. The latter is mainly due to $\Sigma(1385) \to \Lambda\pi^0$, which is one of the significant backgrounds for isolating the $\Lambda(1405)$. Since the Λ and Σ hyperons decay via the weak force, we will call the final states including a hyperon the strong final states. During analysis the hyperons were reconstructed through their weak decay products. The ground-state hyperon decays $\Sigma^+ \to p\pi^0$, $\Sigma^+ \to n\pi^+$, $\Sigma^0 \to \gamma\Lambda \to \gamma p\pi^-$, $\Sigma^- \to n\pi^-$, and $\Lambda \to p\pi^-$ are detected in our analysis.

The analysis procedure was as follows. The raw set of reconstructed and calibrated events was the same as used in several previous CLAS publications [36–39]. We selected events with all of the required charged particles for each channel of interest. After some cuts to reduce backgrounds, described below, a kinematic fit was applied when all final state particles but one were detected. Otherwise, the missing mass squared was computed for the case of the $\Sigma^0\pi^0$ channel. From this, the ground state hyperons of Λ or Σ were reconstructed and selected for analysis in each channel. For brevity, we will label the channels of interest by their ground state hyperon–pion combination, i.e., $\Sigma_p^+\pi^-$, $\Sigma_n^+\pi^-$, $\Sigma^0\pi^0$, $\Sigma^-\pi^+$, and $\Lambda\pi^0$,

where the two Σ^+ decay channels are distinguished with a subscript denoting the final-state baryon. Analyzing both Σ^+ channels served as a cross check of uncertainties introduced by our analysis methods.

A.   Initial selection of particles

The effects of selection cuts discussed below are summarized in Table I. In this analysis all channels of interest have a final state K^+. For the entire data set, the masses of charged particles were calculated from the momenta given by the drift chamber tracks, and the timing given by the RF-corrected tagger timing and TOF scintillator timing. A loose mass cut was made to select events with a kaon candidate, and these were retained for analysis. Events were then required to have all charged particles reconstructed in the fiducial region of the detector, and a few malfunctioning timing detectors were identified and removed. The fiducial region of good acceptance and good Monte Carlo matching was the same as used in previously-published analyses [36–39] of the same data set. Copious non-strangeness events were removed by testing the hypothesis that a candidate K^+ was actually a π^+ or a proton. The leading backgrounds were $\gamma p \to p\pi^+\pi^-$ with nothing missing, $\gamma p \to p\pi^+\pi^-(\pi^0)$ with the π^0 missing, and $\gamma p \to \pi^+\pi^+\pi^-(n)$ with the neutron missing.

Previously-established corrections to the reconstructed tracks were applied, such as momentum corrections for small imperfections in the magnetic field map, and energy losses due to the charged particles traveling through the target and detector material. The incident photon energy was corrected for the known mechanical sagging of the tagger hodoscope. In all cases a timing cut was applied to remove events where a π^+ was misidentified as the K^+ (see below). A primary event vertex cut along the beam direction selected events very cleanly from the LH2 target and rejected events from foils. Minimum momentum cuts based on the identity of the particle (0.3 GeV/c for protons and K^+, 0.1 GeV/c for $\pi^\pm$) were applied.

As most of the background in these channels came from strangeness-free events, cuts on the timing of particles were crucial to correctly select kaons. In the CLAS detector, the distance a charged particle travels through the drift chambers (l), the accelerator RF- and vertex-corrected event start time (t_0), and the time that the particle hit the TOF paddles (t_1) were recorded along with the particle's magnitude of momentum (p). From this information, the measured travel time was calculated as

$$t_{\mathrm{meas}} = t_1 - t_0. \tag{1}$$

Alternatively, we assumed a mass hypothesis for the particle, m_0, and used the measured momentum to calculate the velocity of the particle as

$$\beta_{\mathrm{calc}} = \frac{p}{\sqrt{p^2 + m_0^2}}, \tag{2}$$

Reaction	Strong Final State	Undetected Particles X $K^+ p\,\pi^-(X)$	$K^+\pi^+\pi^-(X)$	Figures

$\gamma + p \rightarrow K^+ + \begin{cases}\Lambda(1405)\\ \Lambda(1520)\end{cases}$

~33% → $\Sigma^+ \pi^-$ | π^0 (52%) | n (48%) | 6b, 8, 9a, 15, 16, 17, 19, 20

~33% → $\Sigma^0 \pi^0$ | $\pi^0 \gamma$ (64%) | | 6a, 12, 17, 21

~33% → $\Sigma^- \pi^+$ | | n (100%) | 9b, 11, 17, 22

6% / 6% / 87%

$\gamma + p \rightarrow K^+ + \Sigma^0(1385) \rightarrow K^+ \Lambda \pi^0$ | π^0 (64%) | | 6a, 7, 13, 14

$\gamma + p \rightarrow K^{*+} + \Sigma^0$ | $\pi^0 \gamma$ (64%) | | 7, 20

$\gamma + p \rightarrow K^{*0} + \Sigma^+$ | π^0 (52%) | n (48%) | 8, 20

FIG. 2. (Color online) Representation of reaction and decay channels used in this analysis. Particles X given in the columns were reconstructed via kinematic fitting or the missing mass determination. Branching fractions are indicated as percentages. The right-most column lists the figures related to the given channel.

TABLE I. The number of events remaining after each selection cut, in 1000's.

Selection	Channel $\Sigma_p^+\pi^-$, $\Lambda\pi^0$, $\Sigma^0\pi^0$		$\Sigma_n^+\pi^-$, $\Sigma^-\pi^+$	
Detected particles	$K^+p\pi^-$		$K^+\pi^+\pi^-$	
Initial kaon selection	64,026		35,627	
Fiducial cuts	31,486		16,662	
Remove false K^+ due to π^+ or p	4,852		10,045	
Loose ΔTOF cuts	3,093		6,576	
Vertex z cut	3,066		6,464	
Minimum $|\vec{p}|$ requirements	3,047		6,233	
Precise ΔTOF cuts	2,415		3,912	
Kinematic fit or MM^2 cut	818	233	1,052	
Selection on ground state hyperon	440	238	76	316	338

and together with the reconstructed flight distance l determined the calculated flight time of the particle as

$$t_{\text{calc}} = \frac{l}{\beta_{\text{calc}}c}. \qquad (3)$$

Taking the difference between these two timing measures gives

$$\Delta\text{TOF} = t_{\text{meas}} - t_{\text{calc}}, \qquad (4)$$

and cuts were applied on this quantity as a function of particle momentum. Figures 3 and 4 show the momentum-dependent cuts applied to select the π^-, π^+, and K^+.

B. Selection of events for analysis

In all channels, the data were divided into 10 bins of energy spanning 100 MeV in the center-of-mass energy W ($= \sqrt{s}$), and 20 angle bins in the center-of-mass kaon angle. All selection cuts and fits to the data were done independently for each bin. For channels with the $\Sigma^\pm\pi^\mp$ combinations, kinematic fits were applied with fixed mass of the undetected neutron or π^0 (one-constraint or 1C fits). This optimized the information based on the measured momenta while balancing the energy and momentum of the reaction.
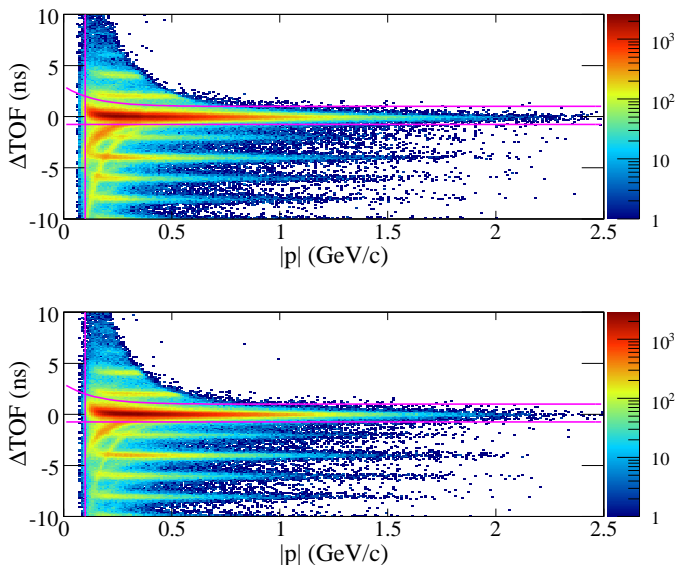
FIG. 3. (Color online) Difference in particle time-of-flight, ΔTOF, versus the measured magnitude of momentum for the π^+ (top) and π^- (bottom) for a given energy bin of $2.35 < W < 2.45$ GeV. The different horizontal bands correspond to the 2 ns time structure of the CEBAF beam. The magenta lines show where the cuts were applied to select each particle.
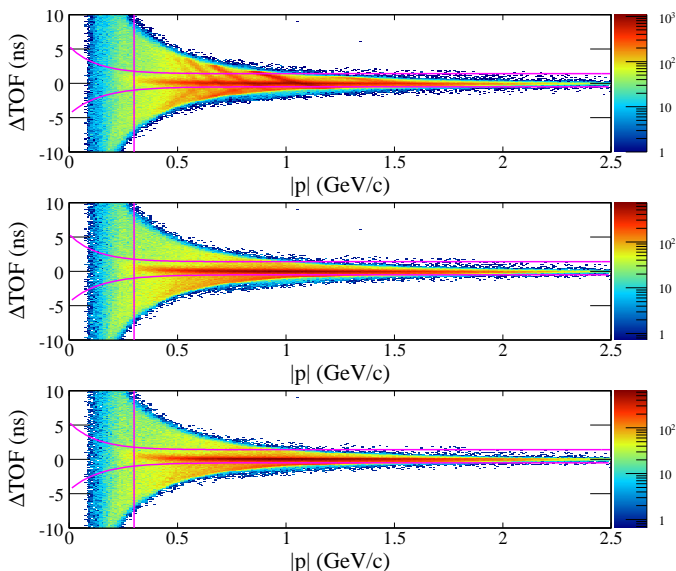

FIG. 4. (Color online) ΔTOF versus the measured magnitude of momentum for the K^+ candidates at several analysis stages for a given energy bin of $2.35 < W < 2.45$ GeV. From top to bottom, the plots correspond to: after the K^+ misidentification rejection cut; after selecting the detected in-time π^- as shown in Fig. 3; and selection on both the detected π^- and π^+. The magenta lines represent the selection cut on the K^+. The last spectrum is seen to be much cleaner after the ΔTOF selection cuts on the pions.

1. Event selection for $\Lambda\pi^0$ and $\Sigma_p^+\pi^-$

In these channels we reconstructed the particles K^+, p, and π^-, with a missing π^0. The 1-C kinematic fit was applied to the selected particles, and those events with a confidence level (CL) of greater than 1% were retained for further analysis. The covariance matrix for these fits was optimized in a previous study [36], and the confidence-level distributions were checked for the present kinematics and found to be very flat. The possible combinations that yield a hyperon in the strong final state are $\Lambda \rightarrow p\pi^-$ and $\Sigma^+ \rightarrow p\pi^0$.

Figure 5 shows the invariant mass squared distributions $\mathrm{M}^2(p\pi^0)$ against $\mathrm{M}^2(p\pi^-)$, summed over all kaon angles in one particular energy bin. For each bin in energy and angle, fits were done to the projections of $\mathrm{M}^2(p\pi^0)$ and $\mathrm{M}^2(p\pi^-)$ with Gaussians and a second order polynomial background. Figure 6 shows a representative example of the fits to the Λ and Σ^+ peaks in a single energy and angle bin. After projecting and fitting the Λ and Σ^+ peaks, a region of $\pm 3\sigma$ was chosen around each peak as the signal region. For further analysis of events with a Σ^+, the overlap region with the Λ was excluded so that there was no Λ distribution underneath the Σ^+ events. On the other hand, because the Λ peak is very narrow (approximately 1.3 MeV/c^2 across all bins when converted to width around the Λ peak, compared to approximately 6.3 MeV/c^2 for the Σ^+ peak), the Σ^+ region was not excluded from the Λ signal, since most of the Λ signal was within this overlap region. The remaining backgrounds were removed as part of the later bin-by-bin yield fits.

For these channels, a small contamination is seen in the projection of the invariant mass squared of the π^- and π^0, which comes from the decay $K^- \rightarrow \pi^-\pi^0$. Since our main channel of interest, the $\Lambda(1405)$, is below the K^-p threshold, we did not cut away this contamination, but removed it later by background subtraction.

After these steps, we arrive at the data set of the strong final states of $K^+\Lambda\pi^0$ and $K^+\Sigma^+\pi^-$. Figures 7 and 8 show the invariant masses of $Y\pi$ against $K^+\pi$, where Y and π are the ground state hyperon and pion in each strong final state, respectively. In each of these Dalitz-like plots there are visible bands due to resonances in the $Y\pi$ system and $K^+\pi$ systems. In the four ranges of W shown, one sees the shifting overlap of the hyperons $\Sigma(1385)$, $\Lambda(1405)$, and $\Lambda(1520)$ versus the K^{*0} and K^{*+}. In Section V the fits to extract the yields of each excited hyperon will be discussed.

2. Event selection for $\Sigma_n^+\pi^-$ and $\Sigma^-\pi^+$

For these channels a final state of $K^+\pi^+\pi^-$ with a missing neutron was required. A kinematic fit to the missing neutron mass was applied to the selected events, retaining those with a confidence level greater than 1%. Again, there are two possible hyperon combinations,
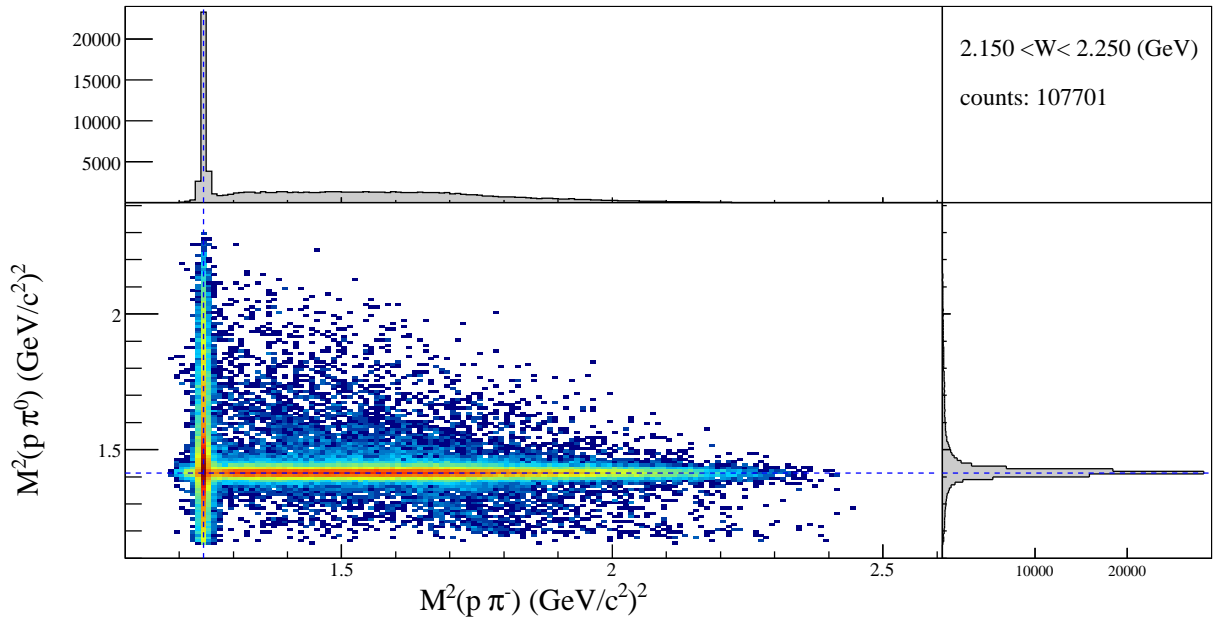
FIG. 5. (Color online) M$^2(p\pi^0)$ versus M$^2(p\pi^-)$ for a given energy bin, with projections. The bands corresponding to the Λ (vertical) and Σ^+ (horizontal) are clearly seen.

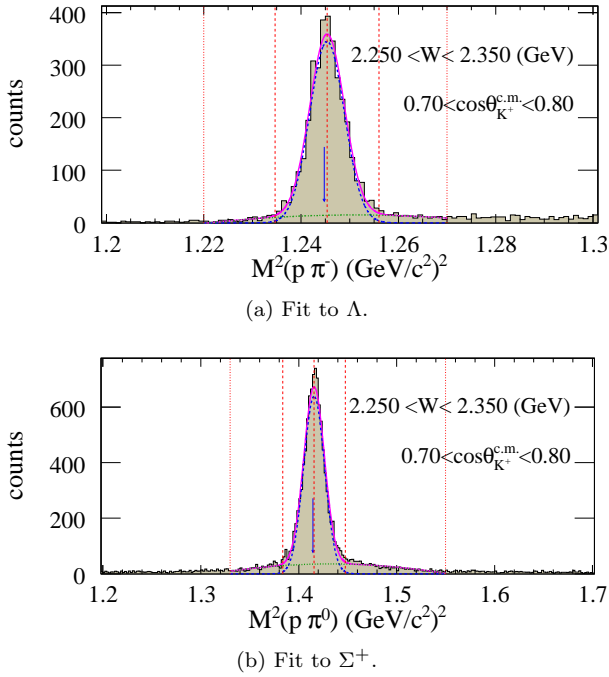(a) Fit to Λ.

(b) Fit to Σ^+.

FIG. 6. (Color online) Fits to the ground state hyperons (a) Λ and (b) Σ^+ for a single bin in energy and angle. The data of each invariant mass squared are shown as the histograms, and the fits are shown as the solid curve (total), dashed curve (Gaussian), and dot-dashed curve (background). The outer dotted vertical lines show the range of the fits, the inner lines show $\pm3\sigma$ around the peaks, which is used to define the signal events.

$\Sigma^{\pm} \to n\pi^{\pm}$, and these correspond to the bands shown in Fig. 9, where the plot of M$^2(n\pi^+)$ versus M$^2(n\pi^-)$ is shown for a particular energy bin.

To isolate the events for Σ^+ (Σ^-), we projected the distributions onto M$^2(n\pi^+)$ (M$^2(n\pi^-)$) and fit the hyperon peaks with a Gaussian and second order background polynomial. Examples are shown in Fig. 10. A region of $\pm2\sigma$ around each peak was chosen as the signal, and the overlap region of the two peaks was excluded from each signal. Also, since there is a band corresponding to $K_S^0 \to \pi^+\pi^-$ events seen in Fig. 9, we followed a similar procedure for M$^2(\pi^+\pi^-)$ and excluded events within $\pm2\sigma$ of the K_S^0 peak also. Figure 11 shows the invariant mass combinations of $\Sigma^-\pi^+$ versus $K^+\pi^+$. Note that in the $K^+\pi^+\Sigma^-$ final state, the combination of $K^+\pi^+$ has no resonant structure. After this selection of $\Sigma^{\pm}$ events, the strong final states of $K^+\Sigma^{\pm}\pi^{\mp}$ were in hand.

3. Event selection for $\Sigma^0\pi^0$

For the $\Sigma^0\pi^0$ channel, the reaction is $\gamma p \to K^+\Sigma^0\pi^0$, with $\Sigma^0 \to \gamma\Lambda$, and $\Lambda \to p\pi^-$. In this case, we were unable to detect the π^0 as well as the γ from the Σ^0 decay, therefore making a kinematic fit impossible. Instead, we fitted the missing mass squared (MM^2) with a Gaussian peak for the π^0 and a second order polynomial for the signal region, and required that MM^2 be more than 3σ above the π^0 peak. Two examples of the selection of MM^2 are shown in Fig. 12, where the selection ranges are shown by the dashed vertical lines.

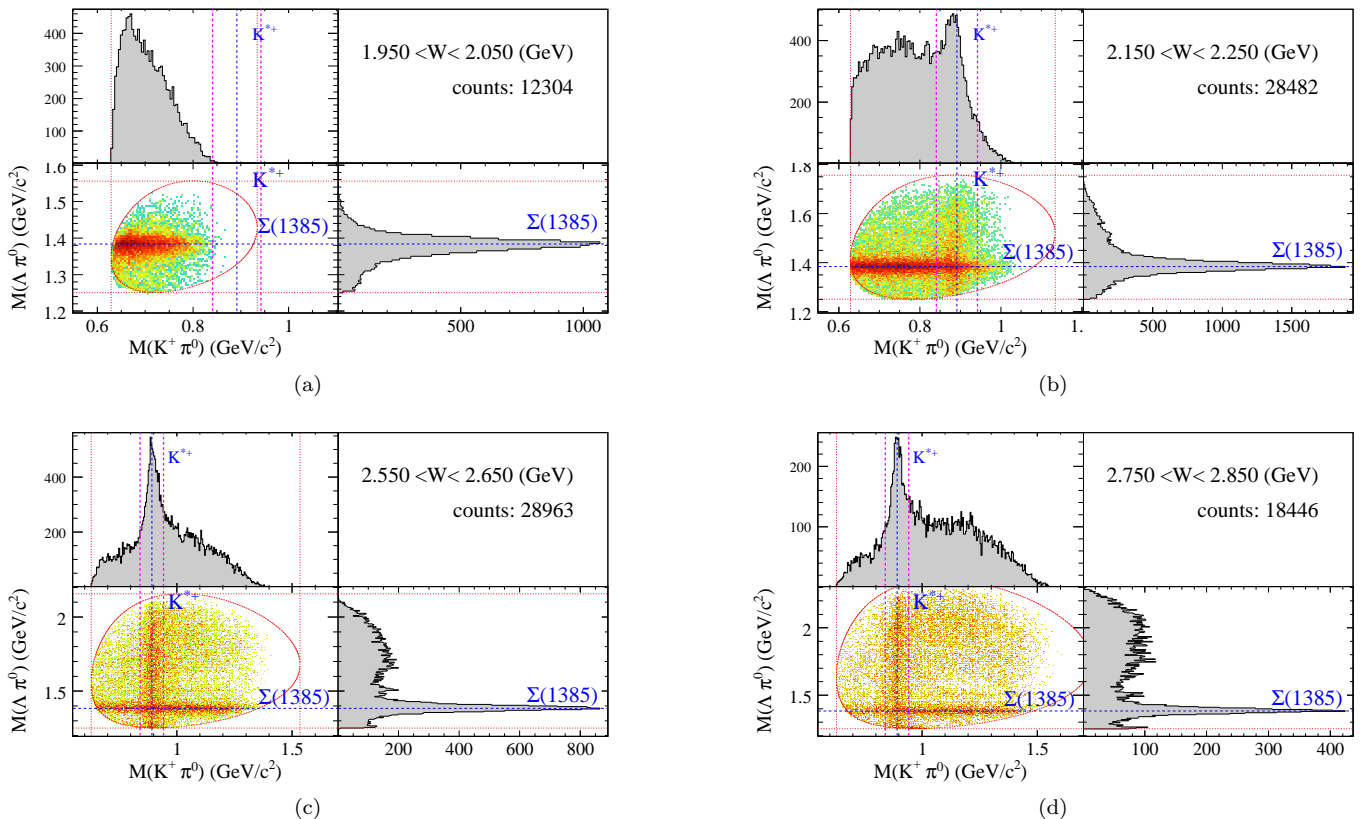To select the Σ^0 events from this channel, the invari-

FIG. 7. (Color online) M($\Lambda\pi^0$) versus M($K^+\pi^0$) for four energy bins increasing from (a) to (d). A clear horizontal band corresponding to the $\Sigma(1385)$ is seen, as well as a vertical band corresponding to the K^{*+}. The contours, as well as the dashed lines, show the kinematic boundaries allowed in that energy bin. The blue dashed lines show the masses of each resonance ($\Sigma(1385)$, K^{*+}) as given by the PDG, while the vertical dashed lines show where the $K^+\pi^0$ invariant mass is $M_0 \pm \Gamma$, and M_0 and Γ are the mass and width of the K^{*+} as given by the PDG.

ant mass squared of the p and π^- was plotted for each bin, and a fit with a Gaussian and a second order polynomial background was performed. The $\pm 3\sigma$ region around the Λ peak was retained. The missing mass off the K^+ then gave the $\Sigma^0\pi^0$ line shape. For the strong final state $K^+\Sigma^0\pi^0$, there are possible hyperon as well as K^{*+} resonances, and in Section V the extraction of hyperon events is discussed.

Table I shows the number of events for each channel after the selections shown in this section. Further selections to isolate the states of interest will be shown later.

IV. ACCEPTANCE AND NORMALIZATION

To understand and correct for the CLAS detector acceptance, a large number of Monte Carlo (MC) events were processed using the GEANT-based standard CLAS simulation package GSIM. After generating the events of interest, the events were passed through the detector simulation, and the momenta were smeared to match the data. An earlier detailed analysis of the g11a data

showed [40] that the trigger condition for this run was not ideally simulated, so an ad hoc trigger efficiency correction of $\sim 5\%$ was applied depending on the event kinematics. After all corrections were made, the simulated events were passed through the same analysis procedures as the data.

One final correction was applied for the events of interest that had a Λ in the strong final state. As mentioned in Section II, the hardware trigger for this run required that two particles register hits in separate sectors of the Start Counter. In the case of an event involving a Λ ($c\tau = 7.89$ cm [25]), there was a small probability of the Λ decaying outside of the Start Counter, and this detail of the trigger was not simulated in software. To remedy this, events in the simulation were removed based on whether the secondary vertex was geometrically outside of the Start Counter. The effect of this correction was stronger at higher energies, and for events with the kaon going backward in the center-of-mass frame, so that for most bins the correction was less than $\sim 3\%$, while for some bins it was as high as 10%. For the other ground-state hyperons Σ^+ and Σ^- ($c\tau = 2.404$ cm and 4.434 cm,
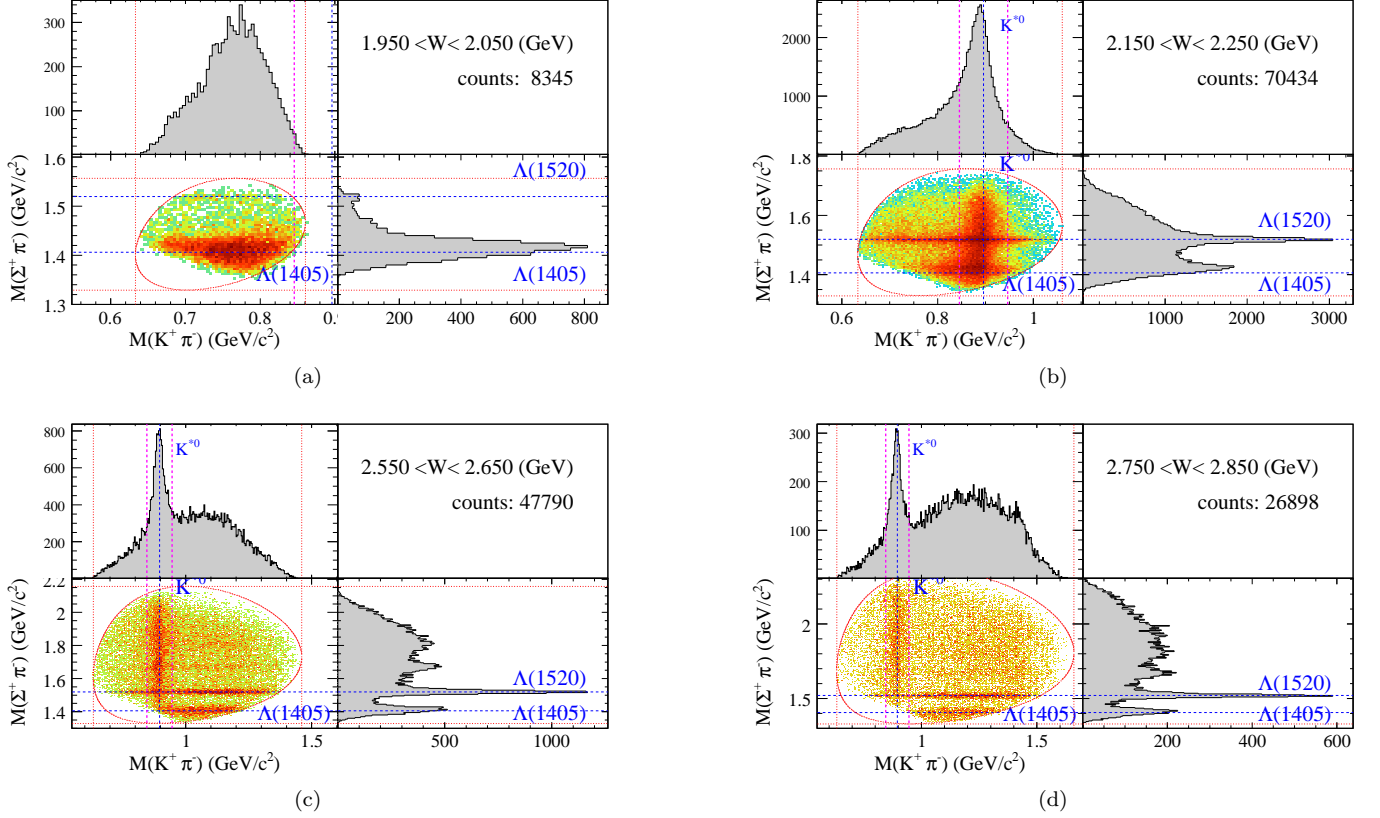
FIG. 8. (Color online) M($\Sigma^+\pi^-$) versus M($K^+\pi^-$) for four bins of increasing energy from (a) to (d). Clear horizontal bands corresponding to the $\Lambda(1405)$, $\Lambda(1520)$, and higher Y^* resonances are seen, as well as a vertical band corresponding to the K^{*0}. The contours as well as the dashed lines show the kinematic boundaries allowed in that energy bin. The blue dashed lines show the masses of each resonance ($\Lambda(1405)$, $\Lambda(1520)$, K^*) as given by the PDG, while the vertical dashed lines show where the $K^+\pi^-$ invariant mass is $M_0 \pm \Gamma$, and M_0 and Γ are the mass and width of the K^{*0} as given by the PDG.

respectively), the effect of the $\Sigma^\pm$ decaying beyond the Start Counter was found to be negligible.

The photon flux in each energy bin was determined so that differential cross sections could be computed. This was done using the CLAS-standard method based on counting out-of-time electrons in the photon tagger within well-defined time windows, and correcting for the measured $\simeq 70\%$ transmission of photons from the tagger to the physics target. Other corrections were made to handle tagger counters not in the primary trigger and to account for the measured $\simeq 85\%$ data acquisition livetime for this data set.

V. YIELD EXTRACTION OF EXCITED HYPERONS

Our method of extracting the strong final state yields used simulations of the signal reaction of interest and of the background reactions in each channel. A fit in the excited hyperon spectrum was performed independently in each bin of center-of-mass energy and kaon angle to

match the data.

As mentioned at the beginning of Section III, we extracted the $\Sigma^0(1385)$ yield in the dominant $\Lambda\pi^0$ decay channel, and with the appropriate acceptance and branching fraction ratios scaled this down to determine the background yields in the $\Sigma^\pm\pi^\mp$ channels. (Note that the $\Sigma^0\pi^0$ channel does not result from $\Sigma^0(1385)$ decay because the isospin coupling coefficient vanishes.) Thus, the $\Sigma^0(1385)$ yield to $\Sigma\pi$ was always known from indirect measurement within any single bin of center-of-mass energy and angle. For this reason, we first discuss extracting the $\Sigma^0(1385) \to \Lambda\pi^0$ events, and then move on to the $\Lambda(1405)$ yields in each $\Sigma\pi$ decay channel.

A. $\Lambda\pi^0$

For the strong final state of $K^+\Lambda\pi^0$, large samples of Monte Carlo events for the reactions $\gamma + p \to K^+ + \Sigma^0(1385)$ and $\gamma + p \to K^{*+} + \Lambda$ were generated and processed. For each bin in center-of-mass energy and kaon angle, the data and Monte Carlo events were kinemati-
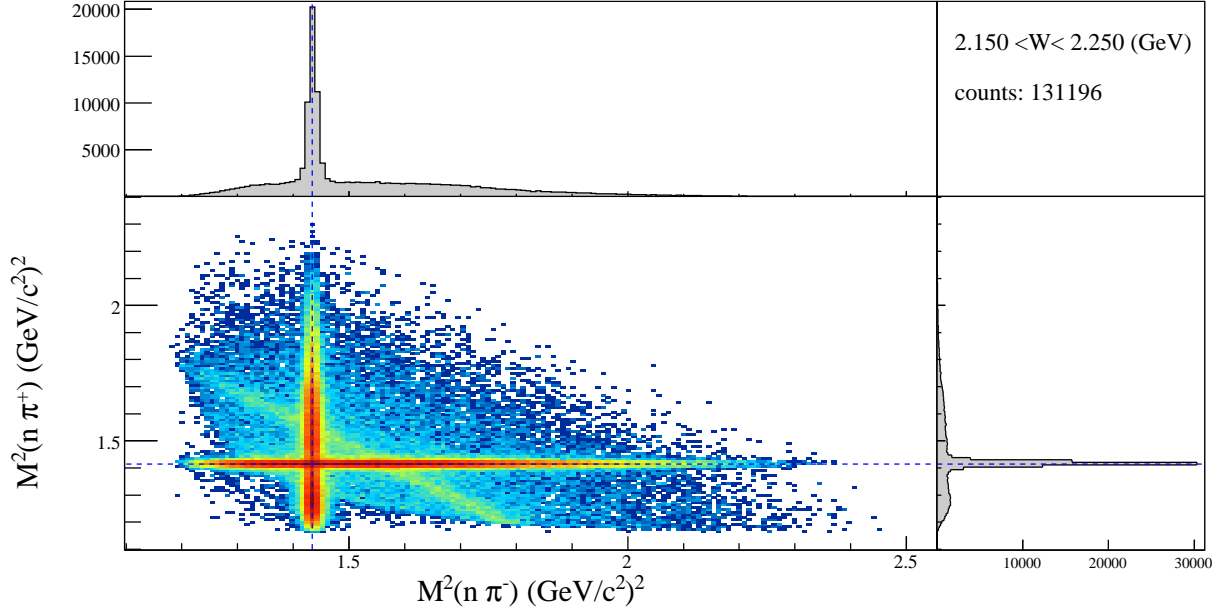
FIG. 9. (Color online) $M^2(n\pi^+)$ against $M^2(n\pi^-)$ for a single energy bin, with projections. The bands corresponding to the Σ^- (vertical) and Σ^+ (horizontal) are clearly seen. The faint diagonal band corresponds to the events of $nK_S^0 \to n\pi^+\pi^-$.

cally fit and plotted as the missing mass from the K^+, which is equivalent to the invariant mass of the Λ and π^0. A fit to the data with these Monte Carlo templates was performed by scaling each Monte Carlo template by an overall factor. Figure 13 shows the fit results for some of these bins. In all bins the $K^{*+}\Lambda$ channel contributes as a smooth background.

A peculiarity was noticed that the $\Sigma(1385)$ line shape could not be fit well using a relativistic Breit-Wigner function with a mass-dependent width. Rather, a non-relativistic Breit-Wigner function with width independent of mass was seen to match the data much better. The line shapes used as input to the CLAS Monte Carlo for counts $dC_x(m)/dm$ as a function of $Y\pi$ mass m were

$$\frac{dC_{\text{non-rel}}(m)}{dm} \sim \frac{\Gamma_0/2\pi}{(m_0 - m)^2 + (\Gamma_0/2)^2} \quad (5)$$

and

$$\frac{dC_{\text{rel}}(m)}{dm} \sim \frac{(2/\pi)mm_0\Gamma(q)}{(m_0^2 - m^2)^2 + (m_0\Gamma(q))^2} \quad (6)$$

for the non-relativistic and relativistic cases, respectively. The mass-dependent width was $\Gamma(q) = \Gamma_0(q/q_0)^{2L+1}$, in which q (q_0) is the breakup momentum of the $\Lambda\pi^0$ or $\Sigma\pi$ system in the resonance rest frame at mass m (m_0). The orbital angular momentum in this case is $L = 1$. Figure 14 shows a comparison of the fit results of the $\Sigma^0(1385)$ peak using Monte Carlo templates generated with the forms of Eqs. 5 and 6. Clearly the relativistic Breit-Wigner template is not able to fit the data well, essentially because the q^3 factor in the numerator suppresses the yield near threshold too much. Therefore

for our present purpose, we used the very simple non-relativistic Breit-Wigner form for fitting the $\Sigma^0(1385)$ data in each bin.

The reason why the non-relativistic Breit-Wigner form fits better to the data is not clear, but we note that previous experiments that determined the $\Sigma(1385)$ mass and width based on hadronic reactions [25], also had difficulties in fitting to a relativistic P-wave Breit-Wigner line shape, and tested non-relativistic forms with mass-independent widths [41–43]. Because these papers measured the charged $\Sigma(1385)$ line shapes, where leakage due to the $\Lambda(1405)$ or other Λ^* states cannot occur, this seems to be an inherent feature of the $\Sigma(1385)$, and not due to some unaccounted leakage in our data. Furthermore, the effect is seen across all of our energy bins, even when below the nominal K^{*+} threshold or when kinematically separated from the K^{*+}. Therefore, we conclude that this effect is not due to interference with the K^{*+} [1].

After the yields of the $\Sigma^0(1385)$ were extracted in each bin of center-of-mass energy and angle, the differential cross sections were calculated using the acceptance based on simulations and the photon flux normalization. The $\Sigma^0(1385)$ differential cross section results will be discussed in a separate paper [32], along with those for the $\Lambda(1405)$ and $\Lambda(1520)$. In this paper we focus on extracting the yields for the $\Lambda(1405)$, for which the yields of the $\Sigma^0(1385)$ decaying to $\Sigma^\pm\pi^\mp$ are necessary.

———————

[1] Refs. [41–43] used the reaction $K^- + p \to \Lambda + \pi^+ + \pi^-$, where there is no K^{*+} background.
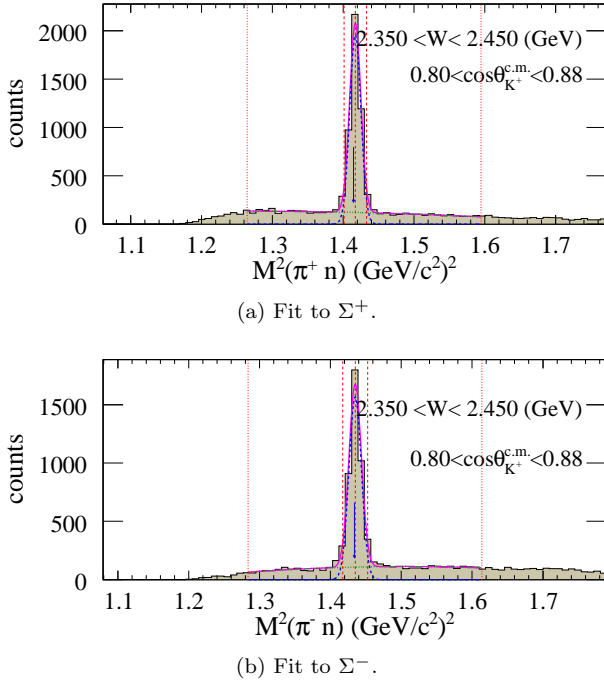
(a) Fit to Σ^+.

(b) Fit to Σ^-.

FIG. 10. (Color online) Fits to the ground state hyperons (a) Σ^+ and (b) Σ^- for a single bin in energy and angle. The data of each invariant mass squared are shown as the histograms, and the fits are shown as the solid curve (total), dashed curve (Gaussian), and dot-dashed curve (background). The outer dotted vertical lines show the range of the fit, and the inner lines show $\pm 2\sigma$ around the peaks used to select events. The opposing signal region was excluded, as well as the $\pm 2\sigma$ peak around the K_S^0.

For each of the charged $\Sigma\pi$ channels, the acceptance-corrected yield of the $\Lambda\pi^0$ channel ($BR = 87.0\%$) was scaled down by using the branching ratio ($BR = 11.7\%$) and acceptance for each bin. Because the $\Sigma^0(1385)$ yield was based on a measurement of the $\Lambda\pi^0$ channel, it was not allowed to vary when extracting the yields of the $\Lambda(1405)$.

B. $\Sigma^+\pi^-$

We next focus on the $\Sigma_p^+\pi^-$ channel, although the other $\Sigma\pi$ channels are quite similar in procedure. As can be seen from the plots of M($\Sigma^+\pi^-$) versus M($K^+\pi^-$) in Fig. 8, there are contributions from the $\Lambda(1405)$, $\Lambda(1520)$, and other excited hyperon states, as well as from the K^{*0}. We model each of these contributions separately with Monte Carlo event templates. Each template is generated according to a relativistic Breit-Wigner form with its resonance mass M_0 and width Γ_0 taken from the PDG [25]. We assumed a mass-dependent width of $\Gamma(M) = \Gamma_0(q/q_0)^{2L+1}$, where q (q_0) is the breakup momentum of the daughter particles in the resonance rest frame at mass M (M_0) with L the orbital angular mo-

mentum. In the fitting procedure, only the normalization of each template was allowed to change to get the best agreement with the data. For the $\Sigma^0(1385)$ contribution, the yield was fixed by the $\Lambda\pi^0$ channel discussed above, and therefore the yield was not allowed to vary.

Figure 15 shows a fit result for the $\Sigma^+\pi^-$ invariant mass spectrum using the above templates for a single bin in center-of-mass energy and angle, along with a background Breit-Wigner function that fits the Y^* resonance around 1670 MeV/c^2. Since our goal is to extract the $\Lambda(1405)$ line shape in the most model-independent way, we start with a relativistic Breit-Wigner form based on the PDG values of mass and width for the $\Lambda(1405)$, and this is shown in Fig. 15(a) as the red points. The fit is inadequate around the $\Lambda(1405)$ region, showing that a simple Breit-Wigner function is not able to describe the data well. For this reason, the template form of the $\Lambda(1405)$ was modified in an iterative way, as explained below.

Once an initial fit was obtained, we subtracted incoherently the contributions due to the $\Sigma^0(1385)$, $\Lambda(1520)$, K^{*0}, and $Y^*(1670)$ so that the only remaining contribution was from what should be the $\Lambda(1405)$. We call this the residual distribution for the $\Lambda(1405)$. Because this residual distribution is the best measure for the raw $\Lambda(1405)$ yield, we applied an acceptance correction based on the Monte Carlo simulation of CLAS. A large number of events was generated flat in the $K^+\Sigma^+\pi^-$ three-body phase space, and the residual distribution was corrected as a function of the $\Sigma^+\pi^-$ invariant mass based on the acceptance of these events. After acceptance correction, the true line shape of the $\Lambda(1405)$ was obtained for each energy and angle bin.

As noted above, the $\Lambda(1405)$ was not adequately described by the initial template, so we used the acceptance-corrected line shape obtained with the above procedure to iterate the Monte Carlo template for the $\Lambda(1405)$ region. The iteration process made use of data summed over all kaon angles within each energy bin. Figure 15(b) shows the third and final iteration. Note that the total fit is now closer to the data, and we see how the iteration converged to stable line shapes based on the data. Since the residual is determined by subtracting off components such as the $\Sigma(1385)$ and the $\Lambda(1520)$, the residual shapes do not depend strongly on the exact template shape we used for the $\Lambda(1405)$. The residual that was obtained from the fit using this final template was acceptance-corrected and normalized to the photon flux, yielding our intermediate result for $d^2\sigma/dm\,d\cos\theta_{K^+}^{\text{c.m.}}$ in bins of energy, angle, and $\Sigma^+\pi^-$ mass m.

The procedure for the $\Sigma_n^+\pi^-$ channel was exactly the same as for the $\Sigma_p^+\pi^-$ channel, because the physics is identical except for the final decay of $\Sigma^+ \to n\pi^+$. Line shapes were obtained in each energy and kaon angle bin. By comparing the two $\Sigma^+\pi^-$ channels we were able to check our results, as will be shown in Section VI.
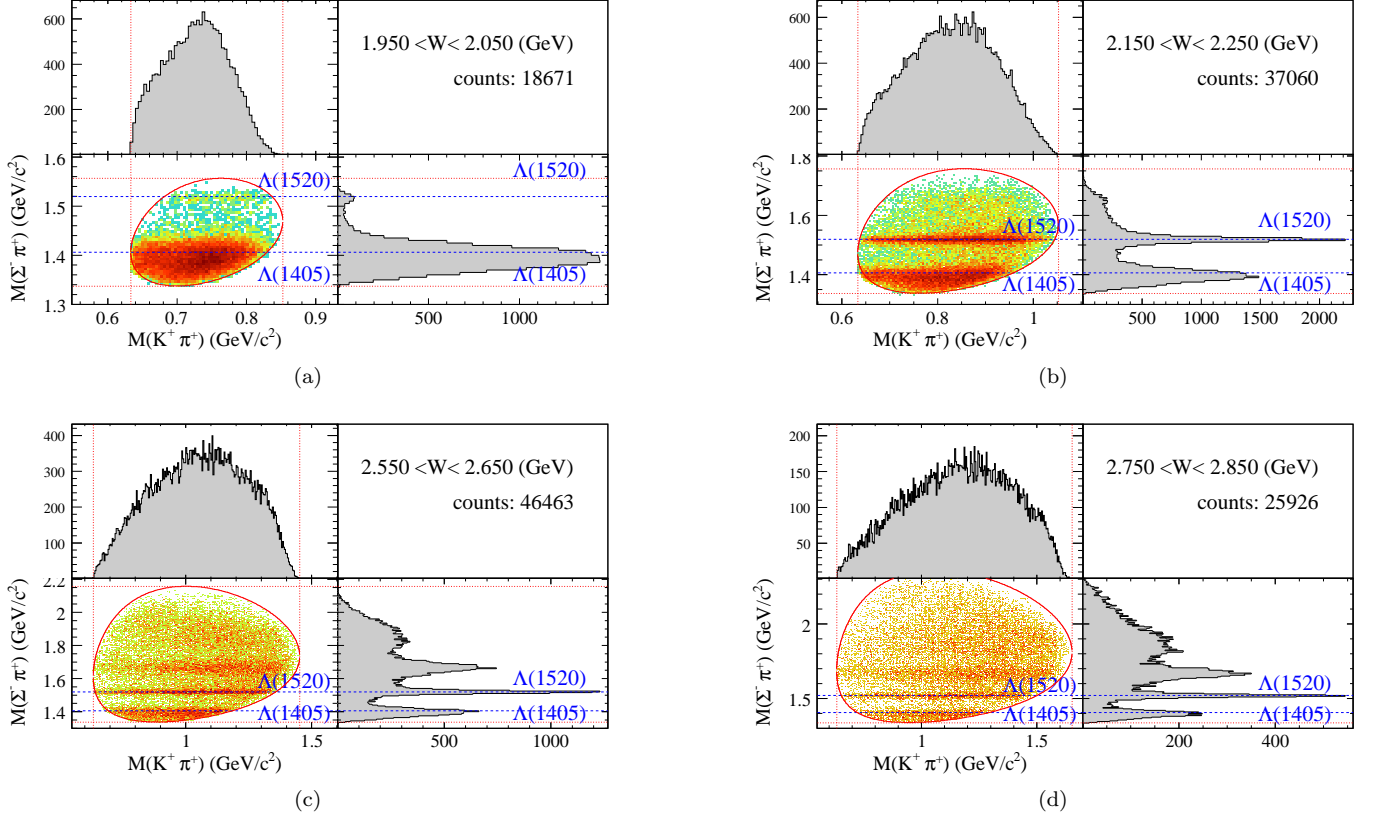
FIG. 11. (Color online) M($\Sigma^-\pi^+$) versus M($K^+\pi^+$) for four energy bins increasing from (a) to (d). Clear horizontal bands corresponding to the $\Lambda(1405)$, $\Lambda(1520)$, and higher Y^* resonances are seen. The blue dashed lines show the nominal masses of the $\Lambda(1405)$ and $\Lambda(1520)$ from the PDG. Note that in this channel the combination of $K^+\pi^+$ shows no resonant structure. The contours as well as the dashed lines show the kinematic boundaries allowed in that energy bin.

C. $\Sigma^-\pi^+$

For the $\Sigma^-\pi^+$ channel, we followed the same procedures as above, but in this case, with the strong final state of $K^+\Sigma^-\pi^+$, the $K\pi$ combination is exotic, and therefore we expect no resonance. However, to accommodate the broadly distributed events seen in Fig. 11, a phase-space distribution of $K^+\Sigma^-\pi^+$ was generated, and this was used as a fit component. The line shapes were iterated as before and then acceptance-corrected.

An interesting feature of this channel is the presence of the $Y^*(1670)$, which shows up much more strongly compared to the other $\Sigma\pi$ channels, as seen in Fig. 11. The PDG lists several candidate resonances in this region, but we have not made an effort to further identify this state.

D. $\Sigma^0\pi^0$

For the remaining $\Sigma^0\pi^0$ channel, we did fits to the K^+ missing mass distribution similar to the previous cases, but since the $\Sigma^0(1385)$ cannot decay to $\Sigma^0\pi^0$ due to the vanishing isospin factor, there is no $\Sigma^0(1385)$ contribu-

tion. The fits were performed with templates for $\Lambda(1405)$, $\Lambda(1520)$, and $K^{*+}\Sigma^0$. As the $Y^*(1670)$ region does not show any prominent peaks, the Breit-Wigner function for $Y^*(1670)$ was not used.

In summary, all $\Sigma\pi$ channels were isolated in order to extract the line shape of the $\Lambda(1405)$ region based on fits to the data. The line shape templates for the region of interest were generated in an iterative way using the data for each channel independently, and in all cases the results showed convergence after several iterations.

VI. LINE SHAPE RESULTS

The $\Sigma\pi$ mass distributions or line shapes, $d\sigma/d\cos\theta_{K^+}^{\mathrm{c.m.}}dm$, were obtained in each bin of center-of-mass energy and kaon production angle, but due to limited statistics we have summed over all angles within each energy bin to obtain a single line shape, $d\sigma/dm$, for each energy bin. Alternatively, we can sum over mass to obtain $d\sigma/d\cos\theta_{K^+}^{\mathrm{c.m.}}$, the differential cross section. These results will be shown in a separate paper. Here we compare the results of the two $\Sigma^+\pi^-$ channels for
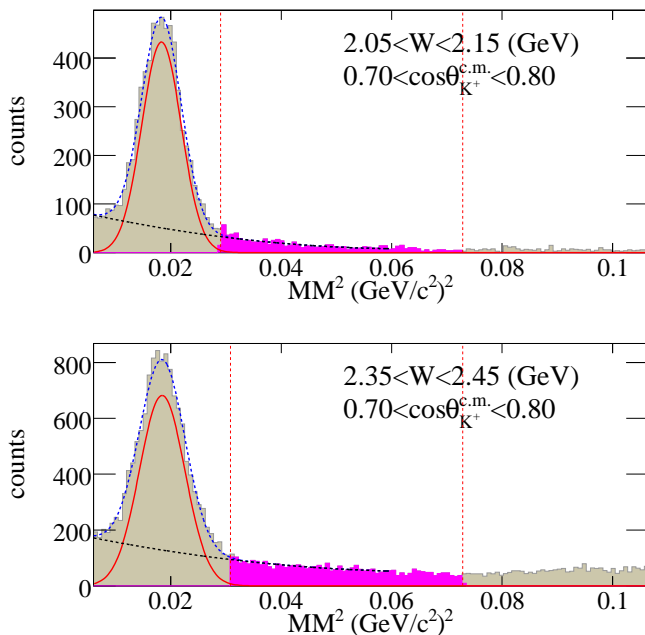
FIG. 12. (Color online) Examples of the $\gamma p \to K^+ p \pi^- (X)$ missing mass squared (MM^2) spectrum for selected kinematic bins. The vertical dashed lines show the selection range for the $\Sigma^0 \pi^0$ channel between the π^0 and $2\pi^0$ limits.

consistency, then proceed to a comparison of all three $\Sigma\pi$ channels.

A. Line shape results for $\Sigma^+\pi^-$ channels

We begin by studying the two channels $\Sigma_p^+ \pi^-$ and $\Sigma_n^+ \pi^-$, which share the same strong final state, and differ only in the decay of the Σ^+. Comparing these two channels gives a measure of the reconstruction accuracy of the analysis. Figure 16 shows a comparison of the line shapes obtained for each $\Sigma^+\pi^-$. channel. The inner error bars are the combined statistical uncertainty of the data and of the Monte Carlo samples that were used in the background subtraction. Our fits to the raw invariant mass spectra using Monte Carlo templates did not always perfectly reproduce the data, even after iterating. To account for this possible systematic error in our analysis, we summed the data within each energy bin over all kaon angles and compared to the summed fit result. Any discrepancy in each mass bin was taken as an additional uncertainty, and a portion was added in quadrature with the statistical errors above. These are shown as the outer error bars in Fig. 16. Thus, the outer errors bars represent the combined point-to-point statistical and systematic uncertainty.

Beyond these estimated uncertainties on single decay modes, any large, possibly-nonstatistical difference between the two measured $\Sigma^+\pi^-$ modes could also signal a systematic discrepancy in the analysis. Therefore, for each mass bin, we took the difference of the two measured

values and subtracted the summed errors in quadrature, obtaining a mass-dependent error that estimates this systematic discrepancy. The shaded histogram at the bottom of the plots shows these uncertainties when the difference of the two measured points is larger than the sum of the two errors. The agreement between the two decay mode reconstruction channels is generally good. The average of these two measurements will be used in the subsequent comparisons with the other charge decay modes.

In all cases the $\Sigma^+\pi^-$ mass distribution clearly peaks at a mass of around 1420 MeV/c^2 which is higher than the nominal mass of the $\Lambda(1405)$ at 1405.1 MeV/c^2 listed by the PDG [25]. We also note the sharp drop or break of the mass distributions at the $N\bar{K}$ threshold near 1.435 GeV/c^2, which is a signature of the opening of a new threshold for S-wave resonances. This will be discussed in Section IX.

B. Line shape results for all $\Sigma\pi$ channels

Our main results [44], the line shape comparison for all three $\Sigma\pi$ channels, is shown in Fig. 17. As noted, the $\Sigma^+\pi^-$ channel is the weighted average of the two measured final states. The $\Sigma^0\pi^0$ channel and $\Sigma^-\pi^+$ channels are again shown with inner and outer error bars, where the inner bars are statistical, and the outer bars include the estimated residual discrepancy in the fits added in quadrature to the inner bars. For each of nine bins in invariant energy W, we show the $\Sigma\pi$ mass distribution in each of three charge states. The data have been summed over the full range of measured kaon production angles. The large-angle cut-offs were not quite identical for all charge states because of differing acceptances, but since the cross sections get very small at large angles ($\cos\theta_{K^+}^{c.m.} < -0.5$) we can neglect these differences.

For all energies, it is evident that the line shapes differ markedly between charge states; in some regions they differ by well over 5σ. This occurs far away from the indicated reaction thresholds, making it unlikely that the effects are due to mere mass differences. None of the mass distributions are reproduced by the simple relativistic Breit-Wigner line shape with PDG-given centroid and width. The $\Sigma^+\pi^-$ channel peaks at a higher mass than the $\Sigma^-\pi^+$ channel, while having a width that is significantly smaller. The charge-dependence of the mass distributions is largest for W between 2.0 and 2.4 GeV. For W approaching 2.8 GeV the mass distributions tend to merge together. This hints that whatever $I \neq 0$ coherent admixture of isospin states is at work here, it fades away at higher total energy. Our own fit to the line shapes to extract our best estimates for the mass and width of the $\Lambda(1405)$ and other structures causing this charge-dependence of the mass distributions will be shown in Section IX.

Comparing our line shape results to the prediction of Nacher *et al.* [7] computed in a chiral unitary model ap-
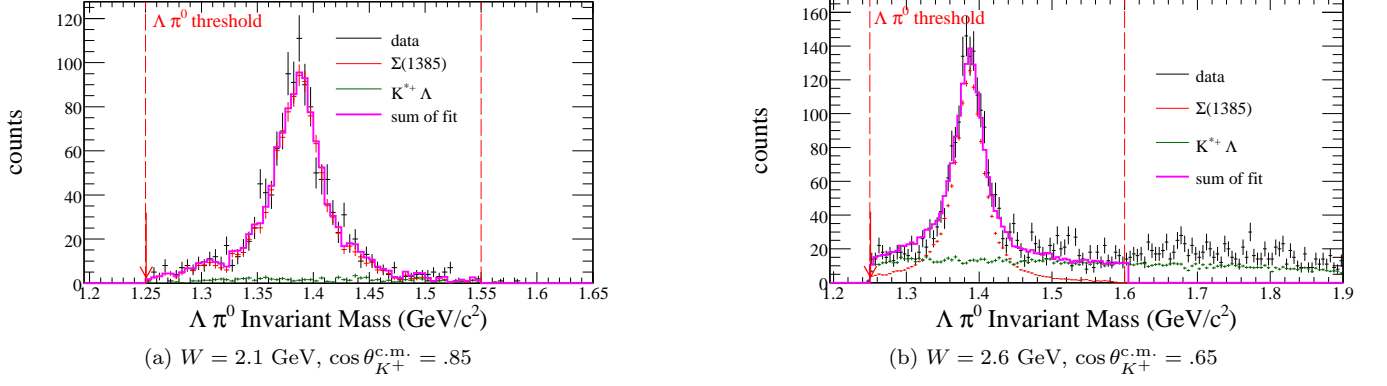
(a) $W = 2.1$ GeV, $\cos\theta^{\mathrm{c.m.}}_{K^+} = .85$

(b) $W = 2.6$ GeV, $\cos\theta^{\mathrm{c.m.}}_{K^+} = .65$

FIG. 13. (Color online) Sample fit results of the strong final state of $K^+\Lambda\pi^0$. The events are plotted versus the missing mass from the K^+, which is equivalent to the invariant mass of the $\Lambda\pi^0$ system. The data are shown by the black crosses, while the $\Sigma^0(1385)$ signal Monte Carlo and the $K^{*+}\Lambda$ background are shown by the red crosses and green circles, respectively. The sum of the Monte Carlo templates are shown by the solid magenta line.
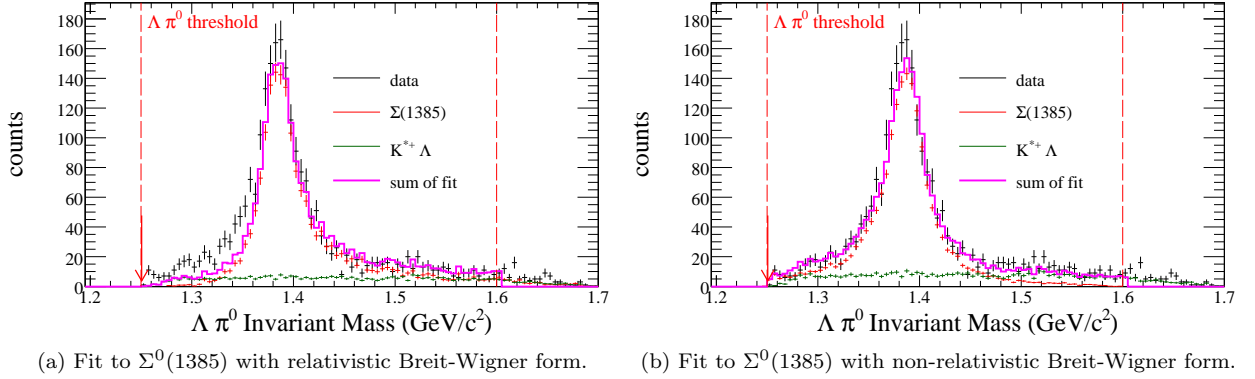

(a) Fit to $\Sigma^0(1385)$ with relativistic Breit-Wigner form.

(b) Fit to $\Sigma^0(1385)$ with non-relativistic Breit-Wigner form.

FIG. 14. (Color online) Sample invariant mass spectra for W = 2.6 GeV and $\cos\theta^{\mathrm{c.m.}}_{K^+} = .65$ showing the $\Sigma^0(1385)$ peak using a Monte Carlo template based on (a) relativistic Breit-Wigner (mass-dependent width) (b) non-relativistic Breit-Wigner (mass-independent width). The fit with the relativistic Breit-Wigner form clearly does not fit the data well.
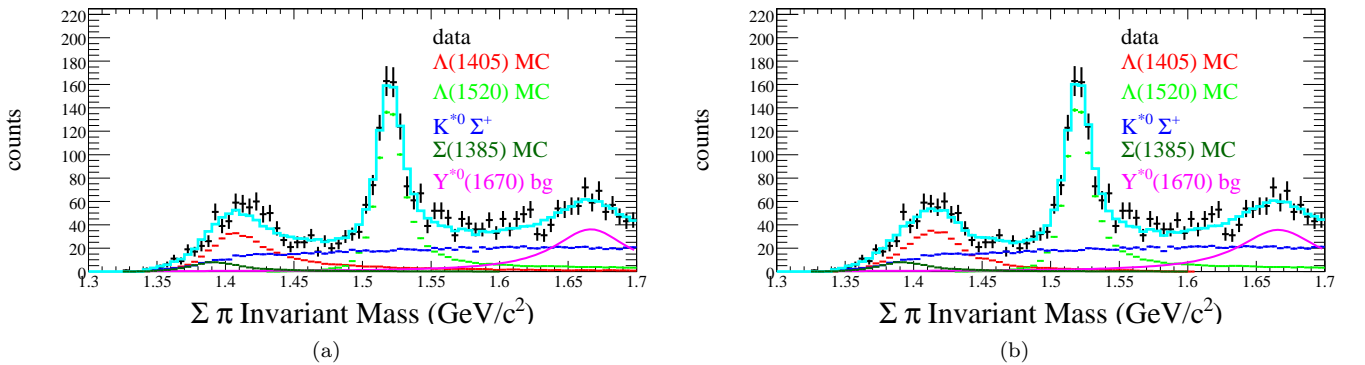

FIG. 15. (Color online) Fit result to the strong final state of $\Sigma^+\pi^-$ before and after Monte Carlo iteration, for $W = 2.5$ GeV, $\cos\theta^{\mathrm{c.m.}}_{K^+} = .35$, as a function of the $\Sigma^+\pi^-$ invariant mass. The data are shown with black crosses. (a) Before iteration. Each Monte Carlo template and the Breit-Wigner function for the $Y^*(1670)$ is shown by a separate color. The total simulation is shown in cyan. (b) After iterations of the $\Lambda(1405)$ template.
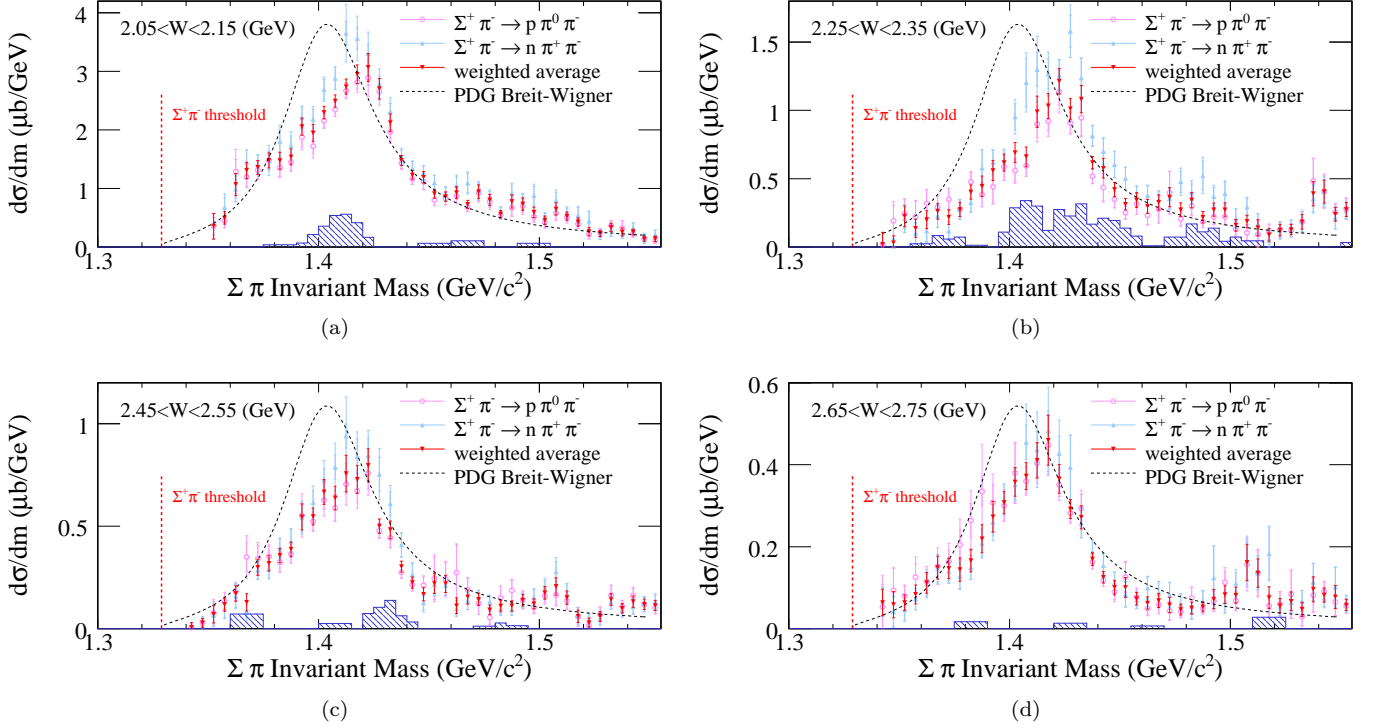
FIG. 16. (Color online) Line shape results for the two $\Sigma^+\pi^-$ channels. The $\Sigma^+_p\pi^-$ channel is shown with light magenta open circles, while the $\Sigma^+_n\pi^-$ channel is shown with light blue triangles. The weighted average of the two line shapes is taken as the final $\Sigma^+\pi^-$ line shape, and is shown as red downward triangles. The dashed line represents a relativistic Breit-Wigner function with a mass-dependent width, with the mass and width taken from the PDG. The blue-hatched histogram at the bottom shows the averaged estimated systematic discrepancy between the two reconstructed decay modes.

proach, we see in Fig. 18 that they are indeed different for each $\Sigma\pi$ channel. In the chiral unitary theory this was explained as an $I = 1$ amplitude interfering with the $I = 0$ $\Lambda(1405)$ amplitude in such a way that the $\Sigma^+\pi^-$ and $\Sigma^-\pi^+$ channels were shifted in opposite directions due to the interference term. The model curves were computed for $E_\gamma = 1.7$ GeV, but we compare with our results at $E_\gamma = 1.88$ GeV since our statistics are better there. The model calculation uses a Weinberg-Tomozawa contact interaction that is energy and angle independent, allowing us to compare the model to the data in any energy bin. In our results it is the $\Sigma^+\pi^-$ channel that is shifted to higher mass with a narrower width, and the $\Sigma^-\pi^+$ channel is smaller and wider, in contrast to the model calculation. Also, the model curves have been scaled down by a factor of 2.0 to match the data, suggesting that the model overestimates the strength of the photocouplings by that amount. In Section IX we will make our own phenomenological isospin decomposition to find a plausible explanation of what is seen.

The other existing prediction for the mass distribution of the $\Sigma\pi$ final states is that of Lutz and Soyeur [11]. In their so-called double kaon pole model, the combined effects of the $\Sigma(1385)$ and the $\Lambda(1405)$ were considered, and this produced some variation among the three charge

combinations we have presented. However, as has been discussed, we subtracted off the effect of the $\Sigma(1385)$ and still are left with a substantial variation in the three final states. We do not compare our results directly to theirs because they are qualitatively similar in shape to those of Ref.[7], and also because they are about a factor of four too large in cross section, indicating a serious quantitative discrepancy when comparing to our results.

VII. SYSTEMATIC UNCERTAINTIES AND TESTS

A. Overall systematics of the run

For systematic uncertainties, there were global contributions from the yield extraction, acceptance corrections, flux normalization, and the line shape fitting procedure. The main cuts that influenced the yield extraction were the ΔTOF cuts, the confidence level cuts in the kinematic fit, and the selection of intermediate the ground-state hyperon. All of these cuts were varied within each bin of center-of-mass energy and angle, and the total yields were checked for any differences due to the cuts. Variation in the ΔTOF width by 0.2 ns changed the acceptance-
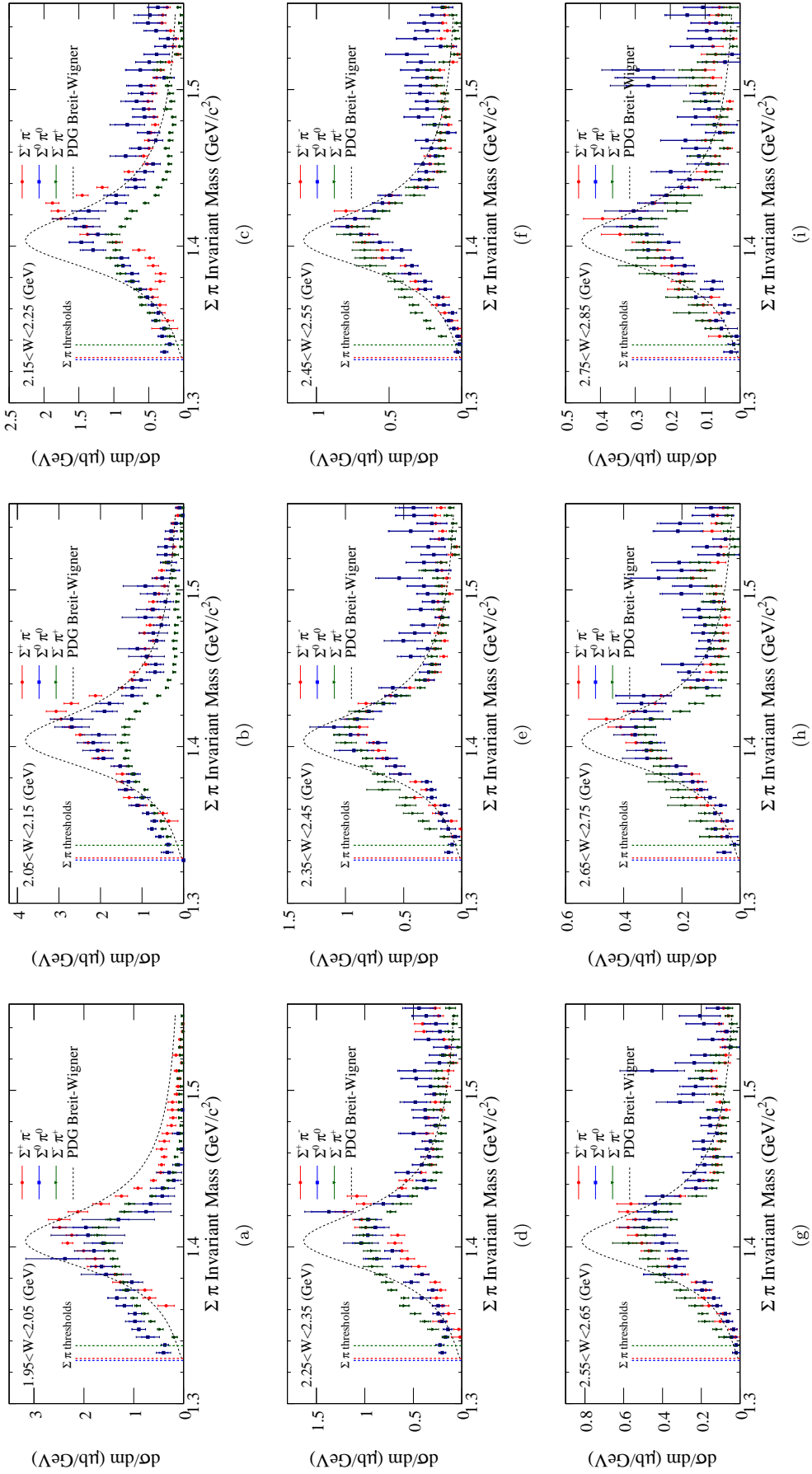
FIG. 17. (Color online) Mass distribution results for all three $\Sigma\pi$ channels. The weighted average of the two $\Sigma^+\pi^-$ channels is shown in the red circles, the $\Sigma^0\pi^0$ channel is shown as the blue squares, and the $\Sigma^-\pi^+$ channel is shown as the green triangles. The $\Sigma^0\pi^0$ and $\Sigma^-\pi^+$ channels have inner error bars representing the statistical errors, and outer error bars that have the estimated residual discrepancy of the data and fit results added in quadrature. The dashed line represents a relativistic Breit-Wigner function with a mass-dependent width, with the mass and width taken from the PDG and with arbitrary normalization. The vertical dashed lines show the opening of each $\Sigma\pi$ threshold.
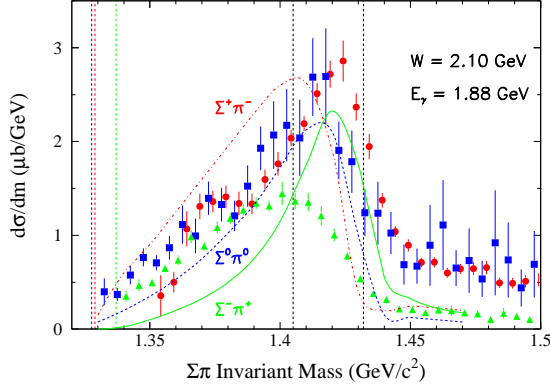
FIG. 18. (Color online) Mass distributions at $W = 2.10$ GeV and $E_\gamma = 1.88$ GeV in comparison to the model of Nacher *et al.* [7] scaled down by a factor of 2.0. The $\Sigma^+\pi^-$ channel is shown as red circles and the red dot-dashed line; the $\Sigma^0\pi^0$ channel is shown as the blue squares and the blue dashed line; the $\Sigma^-\pi^+$ channel is shown as the green triangles and the green solid line. The dashed vertical colored lines at the left side show the reaction thresholds, and the vertical dashed lines at 1.405 GeV and 1.437 GeV mark the nominal centroid and the $N\bar{K}$ thresholds, respectively. The error bars on the data points are combined statistical and point-to-point systematic uncertainties.

corrected yield between 2–6% in each bin. Changing the confidence level from the nominal 1% to 10%, changed the acceptance-corrected yields by 3–12% in each bin. For the majority of the bins, the final yields changed by less than 4% for the ΔTOF cuts, less than 7% for the confidence level cuts, and less than 2% for the ground-state hyperon selection.

Stability of the normalization was monitored throughout the run. The fluctuations in target density were determined to be a negligible 0.11%, while the target length was measured to 0.125%. The photon normalization was examined on an hour-by-hour basis by measuring the ω production yields [37], and the uncertainty for the normalization was determined to be 7.3%. The live-time correction that was necessary to determine the photon flux introduced an additional uncertainty of 3%, and the photon transmission efficiency added 0.5%, so that the total uncertainty for the photon normalization was 7.9.

For the final systematic uncertainty, all of the above global uncertainties were added in quadrature to yield a final value of 11.6%. A summary of each uncertainty is shown in Table II.

The mass resolution of the line shape results was investigated by generating Monte Carlo samples of zero width centered at $\Sigma\pi$ invariant masses of 1.406, 1.450, and 1.500 GeV/c^2. Because the $\Sigma\pi$ invariant mass is equivalent to the missing mass off the detected K^+, the $\Sigma\pi$ mass resolution was related to the momentum resolution of the K^+. However, kinematic fitting of most of the channels

TABLE II. The global systematic uncertainties in the experiment. They arise from yield extraction, acceptance calculation, target characteristics, photon flux normalization, and branching ratios [25]. The total was calculated by summing all in quadrature.

Source	Value
ΔTOF cuts	2–6%
Confidence level on kinematic fit	3–12%
Selection of intermediate hyperons	2–3%
Target density	0.11%
Target length	0.125%
Photon normalization	7.3%
Live-time correction	3%
Photon transmission efficiency	0.5%
$\Sigma(1385) \to \Sigma\pi, \Lambda\pi$	1.5%
$\Lambda \to p\pi^-$	0.5%
$\Sigma^+ \to p\pi^0, n\pi^+$	0.30%
$\Sigma^- \to n\pi^-$	0.005%
Total	11.6%

improved the overall mass resolution. For all generated events in all bins of center-of-mass energy and angle, the $\Sigma\pi$ invariant mass for the accepted events was fit with a Gaussian to determine the resolution. This showed that for the lower energy W bins, the resolution (σ) was better than 6 MeV/c^2, while for the higher energy bins it was up to 8 MeV/c^2, with worse resolution in the backward kaon angles, where the CLAS magnetic field is weaker. Without the kinematic fit, as in the $\Sigma^0\pi^0$ results, the mass resolution averaged about 2 MeV wider at high W and large angles. No shift of the center of the Gaussian larger than 1 MeV/c^2 was seen. Since our results are shown with 5 MeV/c^2 bins, the mass resolution of the line shapes is one to two bins. We also remark that the absolute mass accuracy of the experiment for hyperons such as the $\Sigma(1385)$ and the $\Lambda(1520)$, and of meson states in this mass range is $\lesssim 1$ MeV/c^2.

B. Removal of K^*

A concern in the photoproduction line shape analysis of the $\Lambda(1405)$ region is the effect that the K^* may have. As seen in Fig. 8, the $\Lambda(1405)$ has a kinematic overlap with the K^* in the strong final-state phase space, so that the difference in line shapes seen in the various $\Sigma\pi$ channels could be due to interference with the K^*. Below we argue that this is not the case.

We measure the line shape of the $\Lambda(1405)$ in bins of center-of-mass energy, W, and the kinematic overlap of the K^* depends strongly on this energy. Fig. 8 shows no K^* overlap at low W below the K^* threshold, strong overlap at intermediate W and again no overlap at high W.

We tested for the presence of K^* interference by cut-

ting out regions of $K^+\pi^-$ invariant mass centered around the K^* mass and in multiples of $\Gamma/2$, where Γ is the width of the K^* listed in the PDG. Figure 19(a) shows the effect of each K^* rejection cut up to $\pm\frac{3}{2}\Gamma$ at $W = 2.0$ GeV. For each cut, we reprocessed all of the Monte Carlo samples of the other channels used in the template fit, redid the fit, and applied acceptance corrections. If there were any interference between the K^* and the $\Lambda(1405)$, we would expect it to be strongest in the region where the K^* is strongest, whereas our results show that even with the overlap region removed, the final result is remarkably unchanged by this drastic removal. In Fig. 19(b), the line shape changes significantly only for the cut at $\pm\frac{3}{2}\Gamma$ (green downward triangles), but this is simply due to the loss of phase space and acceptance, since the cut removes about 300 MeV/c^2 of $K^+\pi^-$ invariant mass centered around the K^*. This is reflected in the Dalitz-like plot of the strong final state in Fig. 8, where the boundaries of $\pm\Gamma$ around the K^* mass are shown as vertical dashed lines. Figures 19(c) and 19(d) are more evidence of the insensitivity of the $\Sigma\pi$ mass distributions to the K^*. A similar study was done to test for possible coherent interference between $K^{*+}\Lambda$ and $K^+\Sigma(1385)$, and again no such effect was detected.

We conclude that, although we cannot completely rule out interference due to the K^*, our results are not significantly altered even when we apply a drastic cut on the K^* region, thereby removing most of its strength. Because the photoproduction line shape of the $\Lambda(1405)$ is not known to any accuracy, we do not attempt any further analysis of the interference with the K^*. We anticipate our measurement will further stimulate theoretical interest in this state, and with more theoretical input, a more elaborate analysis may be possible in future experiments.

VIII. MODEL FOR ISOSPIN DECOMPOSITION

We have shown that the line shapes of the $\Sigma\pi$ final states are far from those of a simple Breit-Wigner form. Indeed, there are two main modifications to the picture of a simple single resonance for the $\Lambda(1405)$ mass region

that we will consider in order to gain a reasonable representation of the experimental results. The first arises from the channel-coupling between the detected $\Sigma\pi$ final state and the undetected $N\bar{K}$ final state. This is done by using a Flatté-like formalism [45] to enforce two-channel unitarity and analyticity of the production amplitude. The second arises because we find that the different charge states have markedly different mass distributions, implying that amplitudes other than $I = 0$ must participate in the reaction mechanism. This is treated by including coherent $I = 1$ amplitudes that interfere with the $I = 0$ amplitude.

Since the electromagnetic interaction does not conserve isospin, the initial γp state in this reaction can have both $I = 1/2$ or $3/2$ character, and will lead to a final $K^+(\Sigma\pi)$ state wherein the $\Sigma\pi$ system is in a superposition of $I_{\Sigma\pi} = 0, 1$, and 2 states. The three measured $\Sigma\pi$ final states all have their third component of isospin, $I_{\Sigma\pi}^3$, equal to zero. If we denote the isospin state of the system as $|I_{\pi\Sigma}, I_{\pi\Sigma}^3\rangle$, we can write each of the three measured final charge combinations using Clebsch-Gordon coefficients as

$$|\pi^+\Sigma^-\rangle = \frac{1}{\sqrt{3}}|0,0\rangle + \frac{1}{\sqrt{2}}|1,0\rangle + \frac{1}{\sqrt{6}}|2,0\rangle \quad (7)$$

$$|\pi^0\Sigma^0\rangle = -\frac{1}{\sqrt{3}}|0,0\rangle + 0|1,0\rangle + \sqrt{\frac{2}{3}}|2,0\rangle \quad (8)$$

$$|\pi^-\Sigma^+\rangle = \frac{1}{\sqrt{3}}|0,0\rangle - \frac{1}{\sqrt{2}}|1,0\rangle + \frac{1}{\sqrt{6}}|2,0\rangle. \quad (9)$$

Let t_I be the complex matrix element that takes the initial γp state via a transition operator $\hat{T}^{(I)}$ to the final state that contains the kaon and the $\Sigma\pi$ system in the $I_{\Sigma\pi} = I$ state, so that

$$|t_I|^2 \equiv |\langle I, 0|\hat{T}^{(I)}|\gamma p\rangle|^2. \quad (10)$$

The magnitude-squared matrix element for creating a particular charged final-state pair, $T_{\pi^a\Sigma^b}$ ($a, b \in \{+-, 00, -+\}$), can then be obtained by combining these expressions. For example, the probability of populating the $|\pi^-\Sigma^+\rangle$ state is proportional to

$$|T_{\pi^-\Sigma^+}|^2 \equiv |\langle \pi^-\Sigma^+|\hat{T}^{(0)} + \hat{T}^{(1)} + \hat{T}^{(2)}|\gamma p\rangle|^2 \quad (11)$$

$$= \frac{1}{3}|t_0|^2 + \frac{1}{2}|t_1|^2 + \frac{1}{6}|t_2|^2 - \frac{2}{\sqrt{6}}|t_0||t_1|\cos\phi_{01} - \frac{1}{\sqrt{3}}|t_1||t_2|\cos\phi_{12} + \frac{\sqrt{2}}{3}|t_0||t_2|\cos\phi_{02}, \quad (12)$$

in which the real relative phases between the three isospin amplitudes are $\phi_{01}(m)$, $\phi_{12}(m)$, and $\phi_{02}(m)$. The other two charge combinations have similar forms. Thus there are five real parameters, assuming one phase is set to zero. We expect the matrix element to have the kinematic dependence $T_{\pi^-\Sigma^+} = T_{\pi^-\Sigma^+}(W, m)$, where W is

the available overall center-of-mass invariant energy and m is the $\Sigma\pi$ invariant mass. At a given value of W and m we have three measured cross sections that are proportional to the three quantities $T_{\pi^a\Sigma^b}$, so we cannot determine all five numbers uniquely.

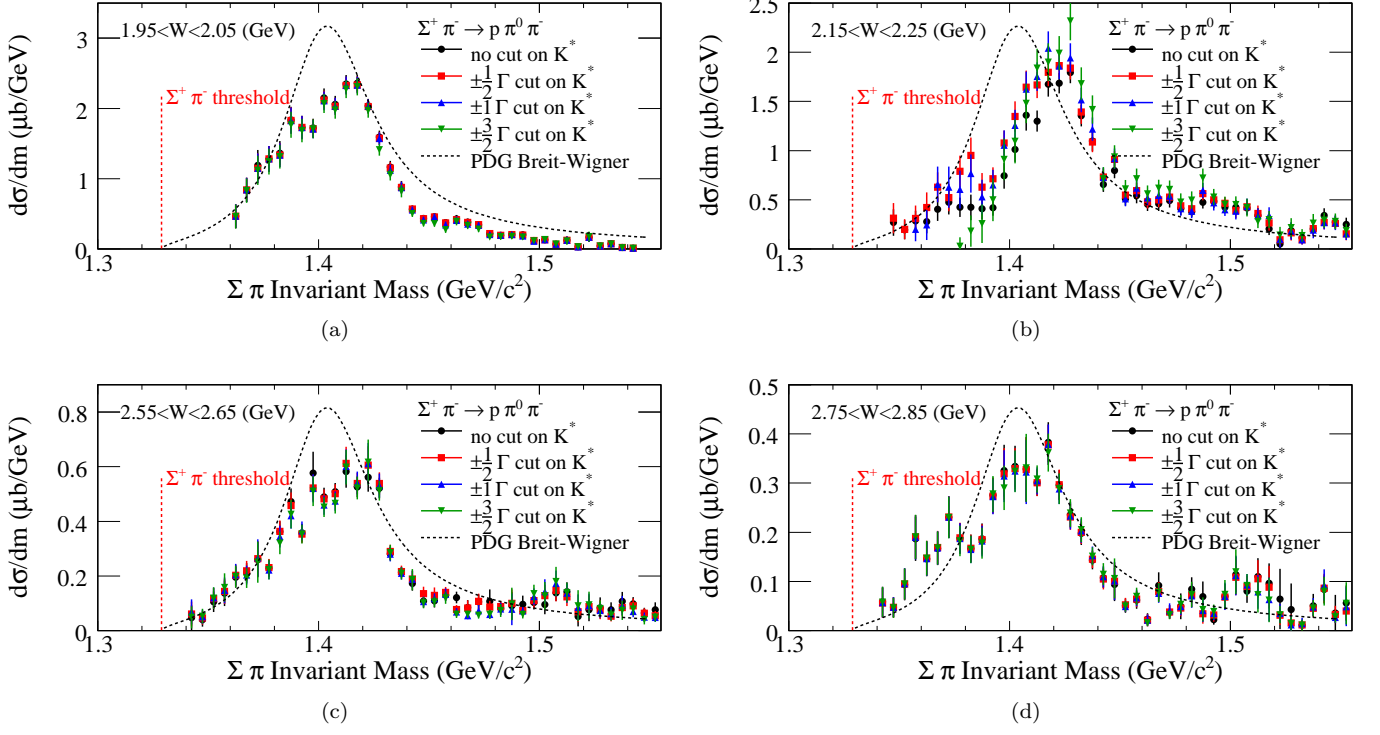Before going on, we chose at this point to apply the as-

FIG. 19. (Color online) Final results for the line shape in the $\Sigma_p^+\pi^-$ channel when the K^* is removed successively in steps of $\pm\frac{1}{2}\Gamma$, where Γ is the width of the K^* quoted in the PDG. The black circles represent our final results without a cut on the K^*, while the red squares, blue triangles, and green downward triangles represent cuts of $\pm\Gamma/2$, $\pm\Gamma$, $\pm\frac{3}{2}\Gamma$ centered around the K^*, respectively.

sumption that the $I = 2$ amplitude is negligible, and that all of the interference in this reaction is between $I = 0$ and $I = 1$ amplitudes only. This assumption is consistent with all previous work on this subject, for example Refs. [7, 9], in which the dynamics of the $\Lambda(1405)$ is presumed to be all within $I = 0$ and/or both $I = 0$ and 1. With this assumption, we can write the expressions for the production strength of the three $\Sigma\pi$ channels as

$$|T_{\pi^-\Sigma^+}|^2 = \frac{1}{3}|t_0|^2 + \frac{1}{2}|t_1|^2 - \frac{2}{\sqrt{6}}|t_0||t_1|\cos\phi_{01}, \tag{13}$$

$$|T_{\pi^0\Sigma^0}|^2 = \frac{1}{3}|t_0|^2, \tag{14}$$

$$|T_{\pi^+\Sigma^-}|^2 = \frac{1}{3}|t_0|^2 + \frac{1}{2}|t_1|^2 + \frac{2}{\sqrt{6}}|t_0||t_1|\cos\phi_{01}. \tag{15}$$

These relationships can be combined to show several things. First, the sum of the measured line shapes gives the sum of the $I = 0$ and $I = 1$ amplitudes' squared magnitudes:

$$|T_{\pi^-\Sigma^+}|^2 + |T_{\pi^0\Sigma^0}|^2 + |T_{\pi^+\Sigma^-}|^2 = |t_0|^2 + |t_1|^2, \tag{16}$$

that is, the interference terms cancel and we see the incoherent sum of the isospin channels. The $I = 0$ amplitude is proportional to the $\Sigma^0\pi^0$ channel alone, as per Eq. (14).

The $I = 1$ amplitude's magnitude squared is given by

$$|t_1|^2 = |T_{\pi^-\Sigma^+}|^2 + |T_{\pi^+\Sigma^-}|^2 - 2|T_{\pi^0\Sigma^0}|^2, \tag{17}$$

which implies that the average of the charged final states should be greater than or equal to the neutral final state, depending on the size of $|t_1|$. The interference between the isospin states is accessed using

$$|T_{\pi^+\Sigma^-}|^2 - |T_{\pi^-\Sigma^+}|^2 = \frac{4}{\sqrt{6}}|t_0||t_1|\cos\phi_{01}. \tag{18}$$

This equation shows how any difference between the charged decay modes is directly related to the interference of the two isospin channels. Note that ϕ_{01} is the mass-dependent phase between $t_0(m)$ and $t_1(m)$. Apart from that mass dependence, we allow an arbitrary strong production phase for each of the amplitudes, called $\Delta\phi_I$ below.

For the production reaction $\gamma + p \to K^+ + (\Sigma\pi)$ we write the contribution from an amplitude of isospin I at fixed γp center-of-mass energy W and $\Sigma\pi$ mass m as

$$t_I(m) = C_I(W)e^{i\Delta\phi_I}B_I(m), \tag{19}$$

where $C_I(W)$ is a real number representing the effective strength of the excitation and $\Delta\phi_I$ is a corresponding

production phase. The Breit-Wigner amplitude has the form

$$B_I(m) = \sqrt{\frac{2}{\pi}} \left[\frac{\sqrt{m_R m \Gamma_I^0 (q/q_R)^{2L}}}{m_R^2 - m^2 - i m_R \Gamma_{\text{tot}}(q)} \right], \quad (20)$$

where m_R is the centroid of the resonance distribution, in this case the $\Sigma\pi$ invariant mass, Γ_I^0 is the fixed decay width to a given final state, and $\Gamma_{\text{tot}}(q)$ is the total width to all final states. The available momentum in the decaying hyperon center-of-mass system is called q, and in this frame q_R is the available decay momentum at $m = m_R$. In this way of writing the amplitude, the numerator has no phase space factor, but this will be included below when we write the final expression for the line shape.

We assume that the line shape for each isospin contribution to the intermediate hyperon state is described by a relativistic Breit-Wigner distribution with suitable phase space factors and normalization. The total width of the resonance, $\Gamma_{\text{tot}}(q)$, is the sum of partial decay widths, but for a single decay channel designated by a "1", let it be the partial decay width $\Gamma_{I,1}(q_1(m))$. The width of the resonance going into a single decay mode "1" is, in the relativistic formulation, dependent on the mass and is written as

$$\Gamma_{\text{tot}}(q) \rightarrow \Gamma_{I,1}(q_1) = \Gamma_{I,1}^0 \frac{m_R}{m} \left(\frac{q_1(m)}{q_R} \right)^{2L+1}, \quad (21)$$

where $\Gamma_{I,1}^0$ denotes a fixed decay width that will be determined by the fit, and $q_1(m)$ is the available momentum in this decay mode at mass m. This expression accounts for the increasing phase space available for the two-body decay across the resonance, and it forces the width to zero at threshold. (Later we will analytically continue q below threshold, however.) We will consider only $L = 0$ or S-wave decays, as required for the odd-parity $\Lambda(1405)$ decaying to a pseudo-scalar meson and an octet baryon.

The overall coupling strength of the resonance represented by Eq. (20) for the reaction $\gamma + p \rightarrow K^+ + \Lambda(1405)$ is given by the parameters in Eq. (19). We take these to be fixed (at a given value of W) over the whole range of the mass distribution m.

For several of the fits to the data (discussed below) we used either two $I = 0$ or two $I = 1$ Breit-Wigner amplitudes. In all cases these amplitudes were added coherently. We selected $\Delta\phi_0$ for the 'first' or 'dominant' $I = 0$ amplitude to be zero, so the other strong phases were determined relative to it.

For hadronic reactions we must also consider the dynamical consequences of the opening of thresholds to decay channels other than the single channel denoted "1". In the present situation there is the $N\bar{K}$ channel that opens at $m_{\text{thresh}} = m_K + m_N \simeq 1434$ MeV/c^2, which is within the range of the mass distribution of the $\Sigma\pi$ system under study. This can significantly impact the line shape of the resonance. To preserve unitarity and the analytic form of the decay amplitude as a mass threshold is crossed, we modify the amplitude of Eq. (20) in

a specific way. If we denote the second decay mode as channel "2", then the total width of the resonance is

$$\Gamma_{\text{tot}}(m) = \Gamma_{I,1}(q_1(m)) + \Gamma_{I,2}(q_2(m)), \quad (22)$$

where the second decay channel is described by the width

$$\Gamma_{I,2}(q) = \Gamma_{I,2}^0 \frac{m_R}{m} \left(\frac{q_2(m)}{q_R} \right)^{2L+1}. \quad (23)$$

Here, $q_2(m)$ is the decay momentum available for decay mode "2" at mass m, and $\Gamma_{I,2}^0$ is the constant factor for the width of this partial decay mode. Below threshold m_{thresh}, the momentum $q_2(m)$ is nominally zero. However, in the Flatté method [45] we analytically continue the momentum to imaginary values, denoting it as $q_2' = -iq_2$ for $m < m_{\text{thresh}}$. Furthermore, we introduce a Flatté parameter for the branching fraction of the decay modes as

$$\gamma = \Gamma_{I,2}^0 / \Gamma_{I,1}^0. \quad (24)$$

Below threshold for decay mode 2, the total decay width is

$$\Gamma_{\text{tot}}(m) = \Gamma_{I,1}(q_1(m)) + i\gamma \Gamma_{I,1}(q_2'(m)), \quad (25)$$

while above the threshold the total decay width is

$$\Gamma_{\text{tot}}(m) = \Gamma_1(q_1(m)) + \gamma \Gamma_1(q_2(m)), \quad (26)$$

and these two expressions are used, respectively, in Eq (20).

Apart from the overall strength C_I and phase $\Delta\phi_I$, there are two free parameters in these expressions for a single resonance: the intrinsic width $\Gamma_{I,1}^0$, and the relative branching fraction between decay modes γ. The fits were made over the whole range of energy W (in nine bins from 2.0 to 2.8 GeV), and these two parameters were fixed to the same value for all W.

The experimental results for kaon-angle integrated mass distributions are in the form of differential cross sections $d\sigma_{ab}/dm$ with $ab \in \{+-, 00, -+\}$; the expression for this cross section includes relevant flux and phase space factors. Fig. 1 illustrates how this reaction requires the use of three-body phase space. To arrive at it we factorize this phase space into two two-body pieces using standard methods [46], the first for the $K^+ Y^*$ hyperon intermediate state of mass m, and the second for the decay of this state into $\Sigma\pi$.

The fully differential form of the cross section is

$$\frac{d\sigma_{ab}}{d\Omega_{K^+} d\Omega_\Sigma dm} = \frac{(\hbar c)^2}{(4\pi)^5} \frac{p_{K^+} q}{p_{\gamma p} s} |T_{\pi^a \Sigma^b}|^2, \quad (27)$$

where the momentum of the kaon in the overall center-of-mass system is p_{K^+}, the momentum in the $\Sigma\pi$ final state is the aforementioned q, and $\sqrt{s} = W$. The invariant production amplitude $T_{\pi\Sigma}$ is defined by Eqs. (13), (14) and (15).

In the experiment we measure the decay distribution of $Y^* \to \Sigma\pi$ over the full solid angle Ω_Σ, so the data are automatically integrated over this variable. Formally, we take $T_{\pi\Sigma}$ to be independent of this decay angle. The reaction is not "flat" with respect to kaon angle, as we know from measurement of the differential cross section $d\sigma/d\Omega_{K^+}$. But for studying the line shapes we are forced to integrate over kaon angle to gain enough statistics for the analysis. We therefore take $T_{\pi\Sigma}$ to be the kaon-angle averaged matrix element and integrate over Ω_{K^+}. Figure 1 shows that there is a vertex involving the photon, and the strength at this vertex must be proportional to $\sqrt{\alpha}$, where α is the fine structure constant. Factoring this out of the matrix element means the previously-defined fit parameters C_I become an effective strong coupling with units of $\sqrt{\text{GeV}}$. The final expression for the differential-in-mass cross sections is then

$$\frac{d\sigma_{ab}}{dm} = \frac{(\hbar c)^2 \alpha}{64\pi^3} \frac{p_{K^+} q}{p_{\gamma p} W^2} |T_{\pi^a \Sigma^b}|^2. \qquad (28)$$

There is an interplay among the phase space factors in front of the matrix element. For a given invariant energy W, $p_{\gamma p}$ is determined. But the possible ranges of p_{K^+} and m are also limited, so the larger p_{K^+} becomes, the smaller m, and therefore the smaller q must be.

In addition to the coherent sum of the isospin components of the line shapes, it was necessary to include a linear background function under each of the $\Sigma\pi$ mass distributions. This sloping background was introduced to represent less-than-perfect subtraction of the backgrounds due, for example, to K^* production or tails of higher mass hyperons. The need for such a background parametrization is seen in the data, which show that in several mass distributions the trend at the high-mass end of the scales is not toward zero, but rather to a constant or even a rising slope. The problem was mainly with the $\Sigma^0\pi^0$ final state, the one for which it was not possible to make a direct experimental measurement of the K^* background, and we had to rely on the Monte Carlo model alone. The slopes of the backgrounds were not fit parameters, but were matched to the differential mass distributions at 1.6 GeV.

IX. ISOSPIN DECOMPOSITION

We can now take the mass distributions found in this analysis and separate the information from the three charge combinations in the $\Sigma\pi$ final states according to $I = 0$ and $I = 1$ components. This is crucial toward the goal of understanding the contribution from the true $\Lambda(1405)$, which is by definition $I = 0$, and anything else happening in the reaction mechanism.

We found that fitting two $I = 0$ amplitudes to just the $\Sigma^0\pi^0$ data led to a very good fit after including the Flatté channel coupling [47]. A "two-pole" explanation of the $\Lambda(1405)$ would favor such a result. The centroids and widths of the $I = 0$ states remained stable when an $I = 1$

amplitude was added to include the $\Sigma^+\pi^-$ and $\Sigma^-\pi^+$ final state combinations. However, it was found that a much better fit could be obtained with a *single* $I = 0$ amplitude and two separate coherent $I = 1$ amplitudes. This is the result we show here. More complete details of the fits will be given in the separate paper [47], but here we present the "best fit" results.

The fits were made to a reduced data set in order to exactly match the kaon angular coverage of the three decay modes, and to remove data points in the vicinity of the $\Lambda(1520)$ where there was evidence (Fig. 17) of less than perfect Monte Carlo matching. There were a total of 34 free parameters and 1128 data points. The reduced χ^2 of the fit was 2.15, the best we achieved with any amplitude combination. Most of the parameters were taken up with the overall strength of each amplitude, C_I, in each W bin. The centroid, width, and Flatté parameters of the fitted amplitudes as per Eq. (19) are given in Table III.

TABLE III. Results of the fit using one $I = 0$ and two $I = 1$ Breit-Wigner line shapes.

Amplitude	Centroid m_R (MeV/c^2)	Width $\Gamma_{I,1}^0$ (MeV/c^2)	Phase $\Delta\Phi_I$ (radians)	Flatté Factor γ
$I = 0$	1338 ± 10	85 ± 10	N/A	0.91 ± 0.20
$I = 1$ (narrow)	1413 ± 10	52 ± 10	2.0 ± 0.2	0.41 ± 0.20
$I = 1$ (broad)	1394 ± 20	149 ± 40	0.1 ± 0.3	N/A

The $I = 0$ piece of the reaction was found in the fit to be at the $\Sigma\pi$ threshold. The fit was flexible enough to let this centroid move smoothly below threshold if necessary, but the fit was optimal with the centroid of the $\Lambda(1405)$, nominally at 1405 MeV/c^2, pushed down to 1338 MeV/c^2. The rising and falling of the line shape is controlled by the opening of phase space from threshold on the low mass side, and by the inflection caused by the opening of the $N\bar{K}$ threshold on the high-mass side. The intrinsic width of the $I = 0$ resonance was fitted to 85 MeV/c^2. However, we expect this width to be poorly determined due to the dominance of the thresholds above and below the centroid. The Flatté coupling parameter is close to unity. A value of 0.91 means there is a strong switch-over to the $N\bar{K}$ decay mode as the available energy exceeds this threshold. This switch-over is consistent with theoretical expectations [9].

Fig. 20 shows only the $\Sigma^+\pi^-$ data and the corresponding fit, including the underlying separate isospin curves. The black solid curve shows the dominant $I = 0$ line shape which is the same for all W bins. It exhibits a distinct edge and change in curvature at the $N\bar{K}$ mass m_{thresh} due to operation of the Flatté effect. It is evident that the data demand this sort of slope discontinuity in the $\Sigma\pi$ distributions. The fit has some problems for $W = 2.1, 2.2$ and 2.3 GeV, where the prominent nar-

rowing around 1400 MeV/c^2 is not reproduced. We have been unable to find a combination of fit parameters and amplitudes that would improve this situation.

One sees in this and the next figures the "narrow" $I = 1$ contribution (dotted lines) plus a second quite "wide" contribution (dashed lines). Only the narrow line was allowed to have a Flatté break at the $N\bar{K}$ threshold, but not the very wide contribution. The centroid, width, and Flatté parameter for this and the other curves are given in Table III.

Analogous to Fig. 20, Fig. 21 shows only the $\Sigma^0\pi^0$ data and corresponding fit, including the underlying separate isospin curves. The $I = 0$ line shape (solid black) is three times the $\Sigma^0\pi^0$ curves (solid blue), as given in Eq. (14), apart from the incoherent background. Here the effect of using two $I = 1$ amplitudes can be considered. This channel is all $I = 0$, but in accommodating the global fit to all channels, the position, strength, and width of the single $I = 0$ piece is affected. The fit is less good than when fitting the $\Sigma^0\pi^0$ final state alone, and of about equal qualitative goodness as when using two $I = 0$ amplitudes and one $I = 1$ amplitude [47]. The $\Sigma^0\pi^0$ channel did not help us discriminate which amplitude combination is superior.

Figure 22 shows only the $\Sigma^-\pi^+$ data with the corresponding fit (solid green), including the underlying separate isospin contributions. In this case the fits are uniformly good across all values of W. The black curves are the same in each panel except for their fitted magnitudes, which are the same in Figs. 20, 21, and 22 at each W.

The fit comfortably accommodates Breit-Wigner-like $I = 1$ structures centered near 1394 and 1413 MeV/c^2. There are no standard quark-model Σ states that would fit this description. The observation at least tentatively suggests evidence for the $I = 1$, $J^P = 1/2^-$, Σ^* state predicted in some extensions of the basic quark model [18]. However, our fit is a phenomenological parametrization of the $I = 1$ amplitude, and not a direct identification of resonant states.

The broad $I = 1$ structure is hard to interpret because it is so wide. It could result from a non-resonant coherent 3-body amplitude present in the reaction mechanism. The fit is substantially better when including this second $I = 1$ amplitude, in fact, it is crucial for providing the separation between the mass distributions in the threshold region of the three charge states.

The component curves for the one $I = 0$ and two $I = 1$ amplitudes contributing to $d\sigma/dm$ are the same in shape, but differ in magnitude, on each panel. It is evident that the $I = 0$ strength is the largest contribution to the reaction, but the two $I = 1$ contributions are far from small in comparison. The magnitudes of the isospin components as a function of W are shown in Fig. 23. These are the real coefficients as per Eq. (19) that enter each Breit-Wigner amplitude (in magnitude). Above 2.2 GeV the $I = 1$ strengths combined are as large as half of the $I = 0$ strength. The relative phase angle of the broad $I = 1$ amplitude is close to zero with respect to the

$I = 0$ amplitude. This means there is no interference between them apart from the Breit-Wigner phase dependence. However the two $I = 1$ amplitudes have a large phase with respect to each other, as given in Table III, and for this we have is no simple explanation.

We think the work discussed above makes the case that the $\Lambda(1405)$, as seen experimentally in photoproduction on the proton, is not an isolated $I = 0$ resonance centered near 1405 MeV/c^2. The observed line shape (or mass distribution) differs in each of the three $\Sigma\pi$ decay modes, which shows that there is substantial $I = 1$ strength in the system. We found it necessary to carefully consider the opening of the $N\bar{K}$ decay mode. We have interpreted the $I = 1$ strength in terms of two Breit-Wigner resonances that interfere with the pure $I = 0$ state $\Lambda(1405)$. After this was done, we arrived at a satisfactory representation of the experimental results. Even our best fit does not reproduce the data fully, and it is difficult to tell whether the remaining discrepancies indicate unresolved systematic issues with the data or additional physics content that we have not identified.

According to our best fit, a narrow $I = 1$ amplitude is a substantial piece of the overall production strength of what has loosely been called the "$\Lambda(1405)$". A wide contribution also appears to be needed. The extra $I = 1$ strength must have $J^P = 1/2^-$ in order to interfere as it does with the $I = 0$ amplitude, the true $\Lambda(1405)$. It must be emphasized that this $I = 1$ strength has nothing to do with the standard $\Sigma^0(1385)$ $J^P = 3/2^+$ since that state was carefully excluded much earlier in the analysis process, both by explicit subtraction and by recognition that it cannot interfere in the present angle-integrated spectra. Although our angular coverage of the hyperon decays is not complete, a majority of the range has been measured.

Assuming we are correct in the identification and assignment of quantum numbers of the Breit-Wigner amplitudes we see, we can discuss them in light of recent theoretical models. First, the low mass of the $I = 0$ amplitude is consistent with predictions of a two-pole structure for the $\Lambda(1405)$, wherein the lower of the two poles is more likely to couple to the $\Sigma\pi$ final state. For example, in the chiral-unitary model of Ramos, Oset and Bennhold [48], the lower-mass pole is at $1390 + i66$ MeV/c^2. However, the same analysis predicts a Σ with $1/2^-$ at $1579 + i274$ MeV/c^2, which is not consistent with the structure we see. In the model of Oller and Meissner [5] the $I = 0$ lower-mass pole is on two Riemann sheets at $1379 - i28$ and $1433 - i11$ MeV/c^2, whereas the $I = 1$ pole is at $1444 - i69$ and $1419 + i42$ MeV/c^2. Hence this latter model is somewhat closer to our results. The meson-exchange model of Haidenbauer et al. [12] also predicts a two-pole structure for the $\Lambda(1405)$ with positions at $1334.3 + i62.3$ MeV/c^2 and $1435.8 + i25.6$ MeV/c^2. The lower of these is at the $\Sigma\pi$ threshold, as found by us in the present fit. When we fit with two $I = 0$ line shapes [47], however, the higher mass centroid does not match the predicted pole position. The resonance pole positions
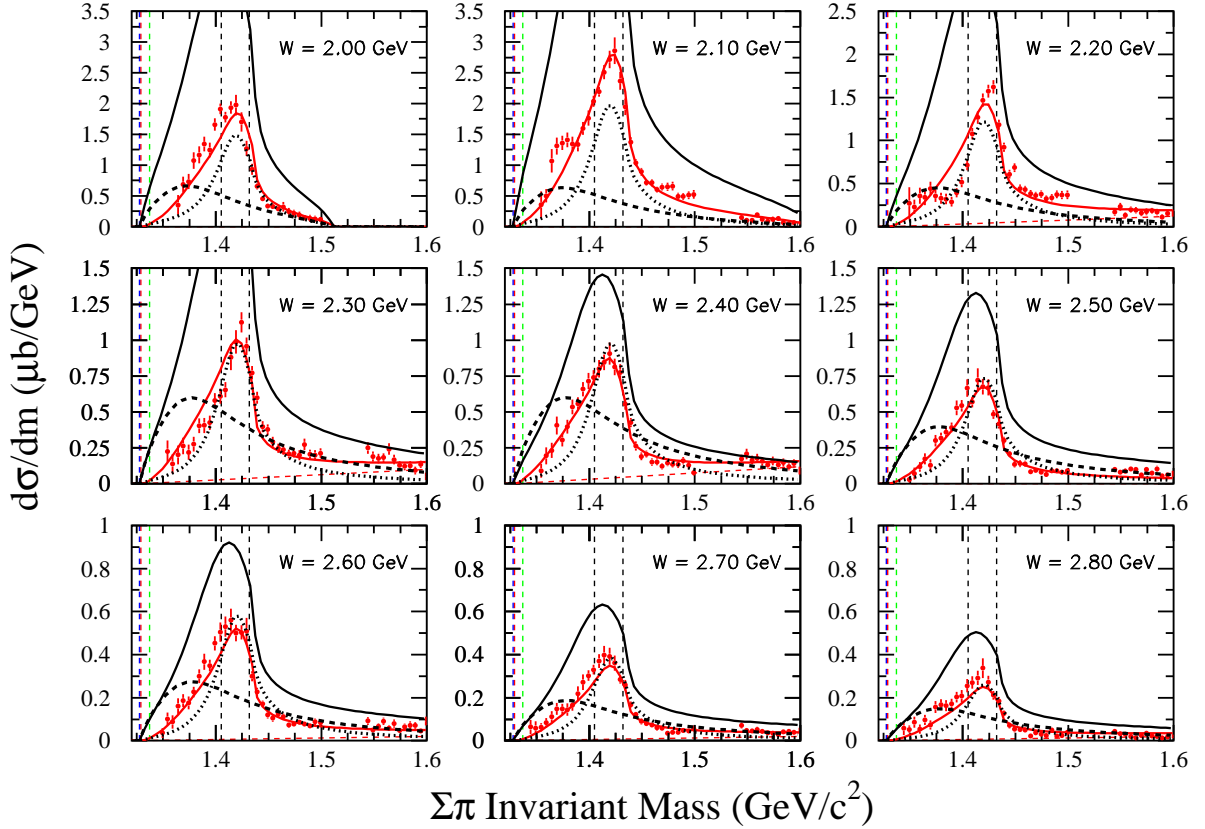
FIG. 20. (Color online) Data and fits for $\Sigma^+\pi^-$, with each panel showing a different value of W. Data and fitted shapes are in red. The isospin contributions are $I = 0$ (solid black), narrow $I = 1$ (dotted black), and wide $I = 1$ (dashed black). The black curves are the same in all panels except for normalization. The vertical dashed lines show the $\Sigma\pi$ thresholds on the left, the nominal 1.405 GeV location, and the $N\bar{K}$ threshold. The incoherent background is shown as a thin dashed line (red).

in the various models do not correspond directly to the centroids of Breit-Wigner mass distributions, so these numerical comparisons are only qualitative.

To make a further connection to previous theoretical work we can make some remarks about previous efforts to identify a $\Sigma^*(1/2^-)$ state near 1380 MeV/c^2. As mentioned in the Introduction, positing such a state was a consequence of examining several open issues in hadron structure using a 5-quark baryon ansatz [18]. In that class of models, the dominant configuration of some excited baryons consists of two diquarks and an anti-quark in a mutual $L = 0$ or $L = 1$ state. This in turn can lead to low mass, negative parity, isovector states such as the one under discussion here. The results we obtained here may relate to the observation that the line shape of the $\Sigma(1385)$ does not conform to its expected P-wave character, as discussed in Section V A. If there is indeed an admixture of an $I = 1$ amplitude with $J^P = 1/2^-$ at nearly the same mass, one can in principle have interferences that modify the line shape of the experimentally-seen $\Lambda\pi$ final state. We have not pursued this question

further at this time. We emphasize once again that a P-wave decay cannot be biasing our results for the S-wave $\Sigma\pi$ data because we integrate over the hyperon decay angles, canceling any interference.

The CLAS results for the $\Sigma\pi$ mass distributions in the vicinity of 1405 MeV/c^2 are compelling in the following sense. The mass distribution differences between the charge states are large and systematic across our measured kinematic space. The need for $I = 1$ strength is inescapable. Furthermore, we have shown that the $\Sigma(1385)(3/2^+)$ is not a player in this phenomenology, and we have taken care to show that the K^* production background also does not play a role. Finally, the line shape fits that we have made show that the $I = 1$ strength is described at least in part by Breit-Wigner $I = 1$ amplitudes with the masses and widths given in Table III.
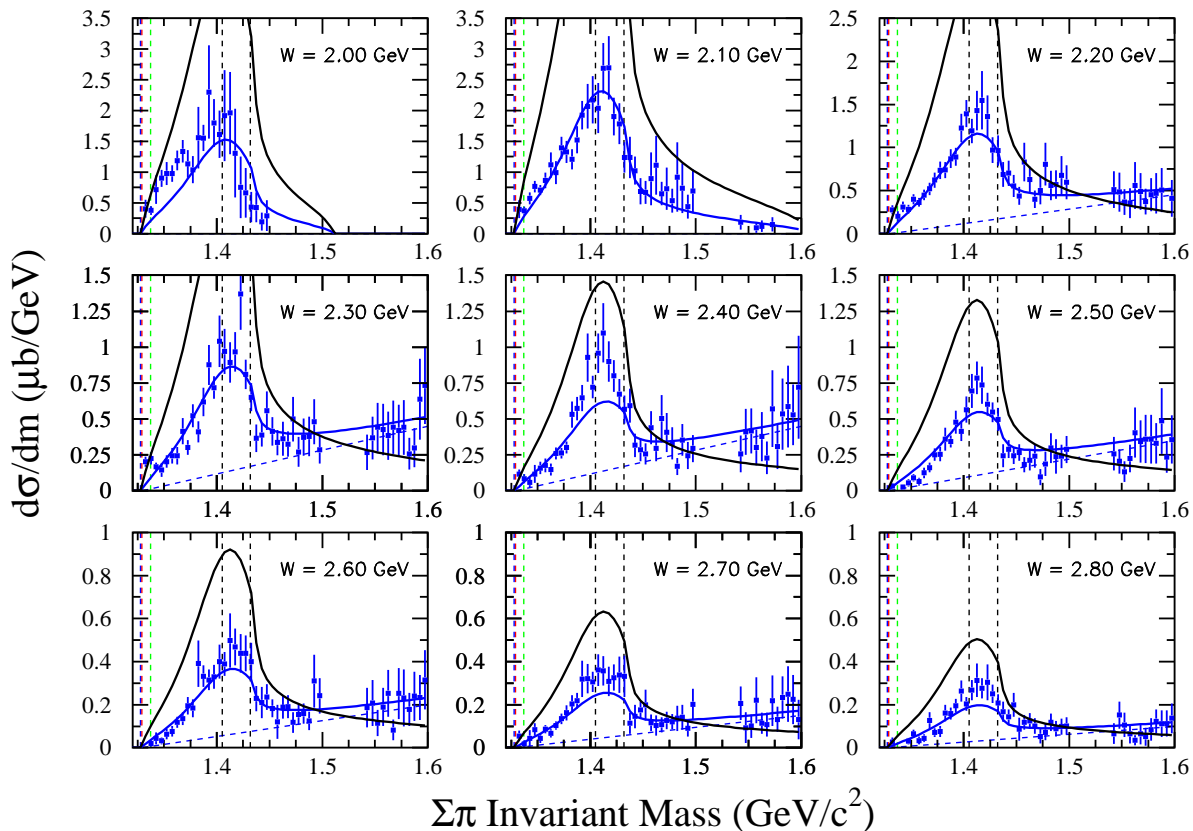
FIG. 21. (Color online) Data and fits for $\Sigma^0\pi^0$, with each panel showing a different value of W. Data and fitted shapes are in blue. All the other lines and curves are exactly the same as in Fig. 20. The $I = 1$ curves are not included here. The incoherent background is shown as a thin dashed line (blue).

X. CONCLUSIONS

The mass distributions or line shapes of the invariant $\Sigma\pi$ mass have been measured in the region of the $\Lambda(1405)$ using CLAS at Jefferson Lab. All three charge combinations were measured, and the main qualitative conclusion is that they are significantly different from each other and none is well represented by a simple Breit-Wigner line shape. We have shown that the background from the $\Sigma(1385) \to \Sigma^\pm\pi^\mp$ states is small and well-controlled by scaling the dominant $\Sigma(1385) \to \Lambda\pi^0$ decay. We have shown that the interference with $K^*\Sigma$ final states is unimportant in the sense that the line shape results are unaffected.

Interference of $I = 0$ and $I = 1$ isospin channels appears to lie at the root of the differing line shapes for the three $\Sigma\pi$ final states. That is to say, there is $I = 1$ strength present with the same $J^P = 1/2^-$ quantum numbers as the $\Lambda(1405)$. Amplitude-level fits suggest that there may be a Σ-like state in this mass range, and that the centroid of the $I = 0$ $\Lambda(1405)$ state lies essentially at the $\Sigma\pi$ threshold. This places the $\Lambda(1405)$ far

from the nominal PDG mass value, in a place where $\Sigma\pi$ threshold effects will have to be understood quantitatively to obtain an accurate picture of this state. From the same analysis, even the $\Sigma^0\pi^0$ channel, which is purely $I = 0$, cannot be represented by a relativistic Breit-Wigner line shape alone. We find that a channel-coupling to the unmeasured $N\bar{K}$ final state via a Flatté-style unitarization can lead to a satisfactory shape, and that indeed this channel-coupling dominates the observed mass distribution. Thus, we find some signature effect for a two-pole picture of the $I = 0$ $\Lambda(1405)$, in which the reaction amplitude couples significantly to both final states. However, we see also how the $I = 1$ amplitude adds one more layer of complexity to the experimental picture by influencing the charged final states. The choice of one $I = 0$ and two $I = 1$ amplitudes presented in this paper led to the best fit among several choices. Similar results were obtained using two $I = 0$ and one $I = 1$ amplitude, which may correspond more closely to current theoretical ideas, but these are described elsewhere [47].

In addition to the results shown in this paper, the photoproduction differential cross sections of the $\Lambda(1405)$,
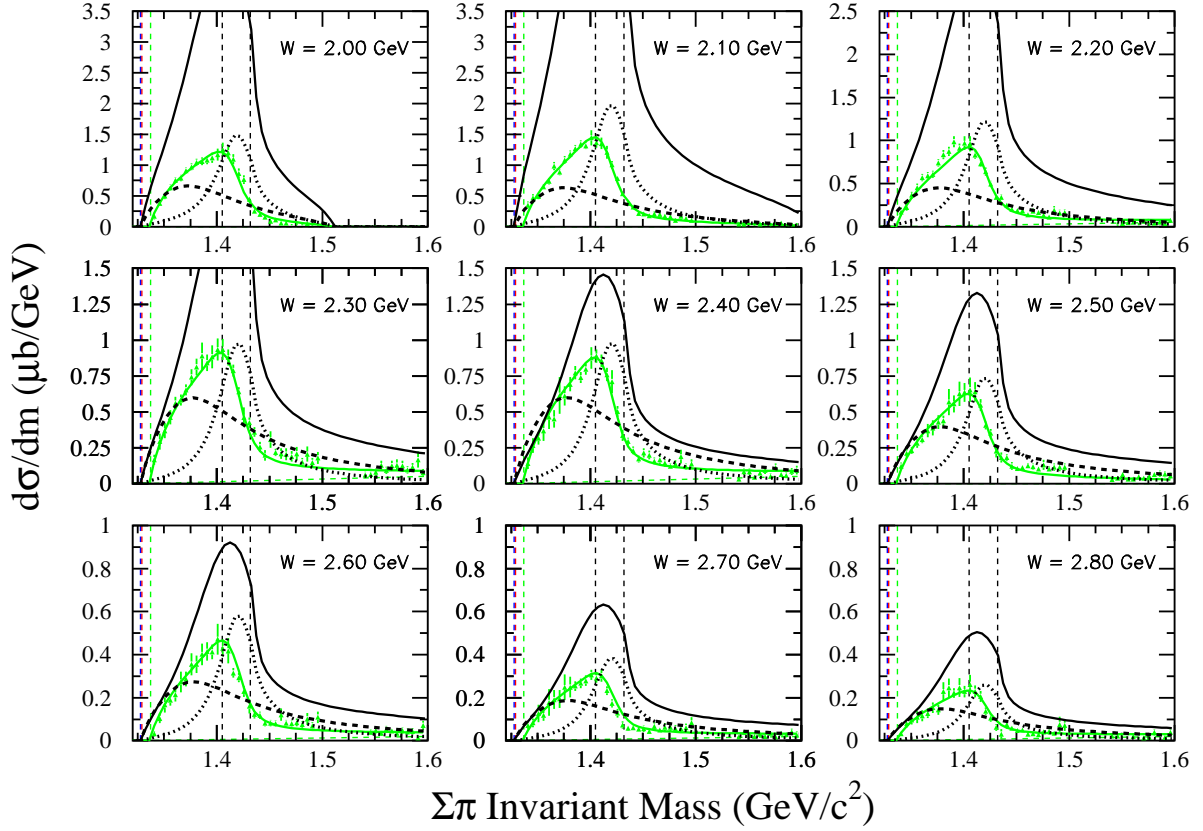
FIG. 22. (Color online) Data and fits for $\Sigma^-\pi^+$, with each panel showing a different value of W. Data and fitted shapes are in green. All the other lines and curves are exactly the same as in Fig. 20. The incoherent background is shown as a thin dashed line (green).
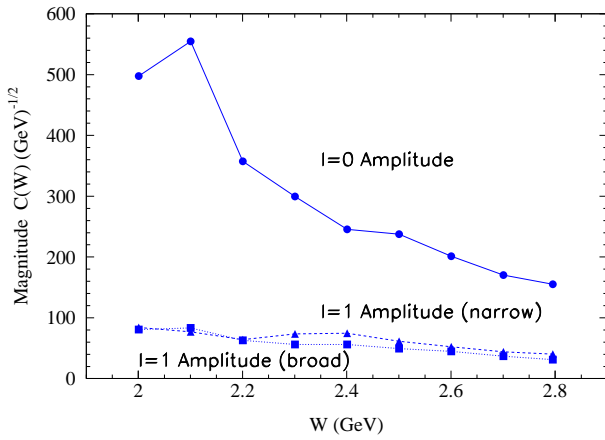

FIG. 23. (Color online) Strength of each of the isospin amplitudes as a function of W. These are the real coefficients of the amplitudes, of which the magnitudes give the contributions of each isospin component.

$\Lambda(1520)$, and $\Sigma(1385)$, will be presented in a separate paper [32]. Also, the same data have been used to directly measure the spin and parity of the $\Lambda(1405)$, and this result will also be presented separately [49].

Clearly, both more theoretical modeling of the present results and additional experimental data are needed. The present work has, we conclude, provided detailed line shape results, to which a parametrization with a set of Breit-Wigner amplitudes shows the importance of $I = 1$, $J^P = 1/2^-$ strength centered near 1394 and 1413 MeV/c^2, with a dominant $I = 0$ piece very near the $\Sigma\pi$ threshold.

ACKNOWLEDGMENTS

[1] M. H. Alston *et al.*, Phys. Rev. Lett. **6**, 698 (1961).
[2] N. Isgur and G. Karl, Phys. Rev. **D18**, 4187 (1978); S. Capstick and N. Isgur, Phys. Rev. **D34**, 2809 (1986); S. Capstick and W. Roberts, Prog.Part.Nucl.Phys. **45**, S241 (2000), arXiv:nucl-th/0008028 [nucl-th].
[3] R. H. Dalitz and S. F. Tuan, Annals Phys. **8**, 100 (1959); Phys. Rev. Lett. **2**, 425 (1959); **10**, 307 (1960).
[4] E. Oset and A. Ramos, Nucl. Phys. **A635**, 99 (1998), arXiv:9711022.
[5] J. A. Oller and U. G. Meissner, Phys. Lett. **B500**, 263 (2001), arXiv:0011146.
[6] T. Hyodo and D. Jido, Prog.Part.Nucl.Phys. **67**, 55 (2012), arXiv:1104.4474 [nucl-th].
[7] J. C. Nacher, E. Oset, H. Toki, and A. Ramos, Phys. Lett. **B455**, 55 (1999), arXiv:9812055.
[8] N. Kaiser, P. B. Siegel, and W. Weise, Nucl. Phys. **A594**, 325 (1995), arXiv:9505043.
[9] D. Jido, J. A. Oller, E. Oset, A. Ramos, and U. G. Meissner, Nucl. Phys. **A725**, 181 (2003), arXiv:0303062.
[10] B. Borasoy, R. Nissler, and W. Weise, Eur. Phys. J. **A25**, 79 (2005), arXiv:0505239.
[11] M. F. Lutz and M. Soyeur, Nucl.Phys. **A748**, 499 (2005), arXiv:nucl-th/0407115 [nucl-th].
[12] J. Haidenbauer, G. Krein, U.-G. Meissner, and L. Tolos, Eur.Phys.J. **A47**, 18 (2011), arXiv:1008.3794 [nucl-th].
[13] Y. Akaishi and T. Yamazaki, Phys. Rev. **C65**, 044005 (2002); Y. Akaishi, T. Yamazaki, M. Obu, and M. Wada, Nucl.Phys. **A835**, 67 (2010), arXiv:1002.2560 [nucl-th].
[14] C. G. Wohl (Particle Data Group), Phys.Rev. **D86**, pp 1383 (1998), article "Charmed Baryons" in Ref. [25].
[15] L. S. Kisslinger and E. M. Henley, Eur.Phys.J. **A47**, 8 (2011), arXiv:0911.1179 [hep-ph].
[16] Kittel, Olaf and Farrar, Glennys R., (2000), arXiv:0010186 [hep-ph]; (2005), arXiv:0508150 [hep-ph].
[17] P. Gao, J. Shi, and B. Zou, Phys.Rev. **C86**, 025201 (2012), arXiv:1206.4210 [nucl-th].
[18] B.-S. Zou, Nucl. Phys. **A835**, 199 (2010), arXiv:1001.1084 [nucl-th].
[19] J.-J. Wu, S. Dulat, and B. S. Zou, Phys. Rev. **D80**, 017503 (2009), arXiv:0906.3950 [hep-ph].
[20] J.-J. Wu, S. Dulat, and B. Zou, Phys.Rev. **C81**, 045210 (2010), arXiv:0909.1380 [hep-ph].
[21] P. Gao, J.-J. Wu, and B. Zou, Phys.Rev. **C81**, 055203 (2010), arXiv:1001.0805 [nucl-th].
[22] K. P. Khemchandani, A. Martinez Torres, H. Kaneko, H. Nagahiro, and A. Hosaka, Phys. Rev. D **84**, 094018 (2011).
[23] Y. Oh, Phys. Rev. D **75**, 074002 (2007).
[24] E. Oset, A. Ramos, and C. Bennhold, Phys.Lett. **B527**, 99 (2002), arXiv:nucl-th/0109006 [nucl-th].
[25] J. Beringer *et al.* (Particle Data Group), Phys.Rev. **D86**, 010001 (2012).
[26] D. W. Thomas, A. Engler, H. E. Fisk, and R. W. Kraemer, Nucl. Phys. **B56**, 15 (1973).
[27] R. J. Hemingway, Nucl. Phys. **B253**, 742 (1985).
[28] I. Zychor *et al.*, Phys. Lett. **B660**, 167 (2008), arXiv:0705.1039 [nucl-ex].
[29] G. Agakishiev *et al.* (HADES), Phys.Rev. **C85**, 035203 (2012), arXiv:1109.6806 [nucl-ex].
[30] J. K. Ahn *et al.* (LEPS), Nucl. Phys. **A721**, 715 (2003).
[31] M. Niiyama *et al.* (LEPS), Phys. Rev. **C78**, 035202 (2008), arXiv:0805.4051 [hep-ex].
[32] K. Moriya and R. A. Schumacher (CLAS), (2013), to be submitted.
[33] D. I. Sober *et al.*, Nucl. Instrum. Meth. **A440**, 263 (2000).
[34] B. A. Mecking *et al.* (CLAS), Nucl. Instrum. Meth. **A503**, 513 (2003).
[35] K. Moriya, Ph.D. Thesis, Carnegie Mellon University (2010), available online at http://www.jlab.org/Hall-B/general/clas_thesis.html.
[36] M. Williams *et al.* (CLAS), Phys. Rev. **C80**, 045213 (2009), arXiv:0909.0616 [nucl-ex].
[37] M. Williams *et al.* (CLAS), Phys. Rev. **C80**, 065208 (2009), arXiv:0908.2910 [nucl-ex].
[38] M. McCracken *et al.* (CLAS), Phys.Rev. **C81**, 025201 (2010), arXiv:0912.4274 [nucl-ex].
[39] B. Dey *et al.* (CLAS), Phys. Rev. **C82**, 025202 (2010), arXiv:1006.0374 [nucl-ex].
[40] M. Williams, Ph.D. Thesis, Carnegie Mellon University (2007), available online at http://www.jlab.org/Hall-B/general/clas_thesis.html.
[41] S. R. Borenstein, G. R. Kalbfleisch, R. C. Strand, V. VanderBurg, and J. W. Chapman, Phys. Rev. **D9**, 3006 (1974).
[42] W. Cameron *et al.* (Rutherford-London), Nucl. Phys. **B143**, 189 (1978).
[43] S. O. Holmgren *et al.* (Amsterdam-CERN-Nijmegen-Oxford), Nucl. Phys. **B119**, 261 (1977).
[44] Full results are available upon request from the lead authors or from the CLAS database at http://clasweb.jlab.org/physicsdb/.
[45] S. M. Flatté, Phys. Lett. **B63**, 224 (1976).
[46] S. U. Chung, (1971), CERN-71-08, Updated version available at http://suchung.web.cern.ch/suchung/spinfm1.pdf.
[47] R. A. Schumacher and K. Moriya, (2012), proceedings of the International Conference on Hypernuclear and Strange Particle Physics XI, Barcelona, Spain, (Submitted to Nucl. Phys. A).
[48] A. Ramos, E. Oset, and C. Bennhold, Nucl.Phys. **A721**, 711 (2003).
[49] K. Moriya and R. A. Schumacher (CLAS), (2013), to be submitted.